

# A depth-averaged $\mu(I)$ -rheology for shallow granular free-surface flows

J. M. N. T. Gray<sup>1,†</sup> and A. N. Edwards<sup>1</sup>

<sup>1</sup>School of Mathematics and Manchester Centre for Nonlinear Dynamics, University of Manchester, Manchester M13 9PL, UK

(Received 28 March 2014; revised 7 July 2014; accepted 30 July 2014)

The  $\mu(I)$ -rheology is a nonlinear viscous law, with a strain-rate invariant and pressure-dependent viscosity, that has proved to be effective at modelling dry granular flows in the intermediate range of the inertial number,  $I$ . This paper shows how to incorporate the rheology into depth-averaged granular avalanche models. To leading order, the rheology generates an effective basal friction, which is equivalent to a rough bed friction law. A depth-averaged viscous-like term can be derived by integrating the in-plane deviatoric stress through the avalanche depth, using pressure and velocity profiles from a steady-uniform solution to the full  $\mu(I)$ -rheology. The resulting viscosity is proportional to the thickness to the three halves power, with a coefficient of proportionality that is angle dependent. When substituted into the depth-averaged momentum balance this term generates second-order derivatives of the depth-averaged velocity, which are multiplied by a small parameter. Its inclusion therefore represents a singular perturbation to the equations. It is shown that a granular front propagating down a rough inclined plane is completely unaffected by the rheology, but, discontinuities, which naturally develop in inviscid roll-wave solutions, are smoothed out. By comparison with existing experimental data, it is shown that the depth-averaged  $\mu(I)$ -rheology accurately predicts the growth rate of spatial instabilities to steady-uniform flow, as well as the dependence of the cutoff frequency on the Froude number and inclination angle. This provides strong evidence that, in the steady-uniform flow regime, the predicted decrease in the viscosity with increasing slope is correct. Outside the range of angles where steady-uniform flows develop, the viscosity becomes negative, which implies that the equations are ill-posed. This is a signature of the ill-posedness of the full  $\mu(I)$ -rheology at both high and low inertial numbers. The depth-averaged  $\mu(I)$ -rheology therefore cannot be used outside the valid range of angles without additional regularization.

**Key words:** granular media, rheology, surface gravity waves

---

## 1. Introduction

Avalanche models have proved to be very successful at predicting many types of phenomena in shallow granular free-surface flows. The earliest published application dates back to Grigorian, Eglit & Iakimov (1967) who used a modified

† Email address for correspondence: [nico.gray@manchester.ac.uk](mailto:nico.gray@manchester.ac.uk)

shallow-water-type theory to compute snow avalanche paths in the Ural Mountains. A formal derivation of the equations was first presented by Savage & Hutter (1989). They depth-averaged the mass and momentum equations, assuming a Mohr–Coulomb internal rheology and a constant Coulomb basal friction law, which produced a system of conservation laws that looked like the shallow-water equations with source terms. An additional complexity was that the depth-averaged pressure gradient was multiplied by an earth pressure coefficient, which changed its value dependent on whether the downslope flow was diverging or converging. Savage & Hutter (1991) and Greve & Hutter (1993) showed that these equations were able to predict the motion of a finite mass of granular material from initiation to run-out on a slope with variable topography. Subsequent models have been generalized to two-dimensional flows over complex topography (e.g. Gray, Wieland & Hutter 1999; Wieland, Gray & Hutter 1999; Mangeney-Castelnau *et al.* 2003; Pudasaini & Hutter 2003; Bouchut & Westdickenberg 2004; Luca *et al.* 2009) and have been extensively used in the snow avalanche community for hazard zone mapping in alpine regions (e.g. Sampl & Zwinger 2004; Christen, Kowalski & Bartelt 2010; Fischer, Kowalski & Pudasaini 2012). Closely analogous theories have also been developed for other hazardous geophysical mass flows, including for debris flows (e.g. Iverson 1997; Denlinger & Iverson 2001; Iverson & Denlinger 2001), pyroclastic flows (e.g. Pitman *et al.* 2003; Doyle, Hogg & Mader 2011) and landslides (e.g. Kuo *et al.* 2009; Mangeney *et al.* 2010).

Gray, Tai & Noelle (2003) simplified the equations by assuming that the in-plane deviatoric stresses were sufficiently small that they could be neglected. This reduced the Savage & Hutter (1989) type models to a shallow-water structure with source terms. By using shock capturing numerical methods (Tai *et al.* 2002) it was possible to use these hyperbolic theories to accurately calculate high-speed granular flows past obstacles, such as pyramids (Gray *et al.* 2003), wedges (Hákonardóttir & Hogg 2005; Cui, Gray & Jóhannesson 2007), constrictions (Vreman *et al.* 2007; Gray & Cui 2007) and cylinders (Cui & Gray 2013), where shock waves developed. This has an important practical application to the design of avalanche defences such as catching and deflecting dams (Barbolini *et al.* 2009), which are used to protect people and infrastructure in mountainous regions. Understanding the flow around such obstacles is also important for the interpretation of data collected at the instrumented pylon at the European Avalanche avalanche test site in the Vallée de la Sionne (Sovilla *et al.* 2008).

Pouliquen (1999a) made systematic measurements of the relationship between the slope angle, the flow depth and the depth-averaged velocity for steady-uniform flows on rough beds. He was able to collapse the data to determine a new rate-dependent friction law, to replace the rate-independent Coulomb friction law used by Savage & Hutter (1989). As a result he was able to calculate the shape of a granular flow front as it propagated down a rough inclined plane, and showed that it agreed remarkably well with experiments (Pouliquen 1999b). An improved version of this basal friction law, which accounted for the friction at low Froude numbers, was given by Pouliquen & Forterre (2002).

Forterre & Pouliquen (2003) investigated the spatial stability of steady-uniform flow, by imposing a controlled perturbation at the inlet and measuring its development down the chute. In this way they were able to experimentally determine the threshold and the dispersion relation of the instability. The results were compared with a linear stability analysis of the problem, within the framework of depth-averaged Saint-Venant (shallow-water) equations with a rough bed friction law. The theory

was able to quantitatively predict the stability threshold and the phase velocity of the waves, but failed to predict the cutoff frequency. Instead, it predicted that the growth rate tended to a positive constant at high frequencies, which indicated that an important dissipative mechanism was missing in the theory. Such instabilities to steady-uniform flow lead to the formation of periodic granular roll waves, such as those shown in figure 1. Roll waves therefore provide a sensitive case against which to test new rheological laws and model formulations. An even more sensitive problem, that is also deserving of study, is that of particle-size segregation-induced fingering instabilities (Pouliquen, Delour & Savage 1997; Pouliquen & Vallance 1999), which cause the classical shallow-water type models to become ill-posed (Woodhouse *et al.* 2012) when coupled to a simple depth-averaged theory for large particle transport (Gray & Kokelaar 2010*a,b*).

The Groupement de Recherche Milieux Divisés (GDR-MiDi 2004) collated experimental data and numerical results, from molecular dynamics and contact dynamics simulations, in six different configurations, with a view to determining the rheology of dense granular flows. Using dimensional analysis they identified two independent non-dimensional parameters in these systems; the effective-friction coefficient  $\mu_{\text{eff}}$ , which is just the ratio of the shear stress to the confining pressure, and the inertial number  $I$ , which is the ratio of a typical time-scale for particle rearrangement to a typical time scale for deformation. This suggested a simple local rheology,  $\mu_{\text{eff}} = \mu(I)$ , in which the effective friction was a function,  $\mu$ , of the inertial number,  $I$ . GDR-MiDi (2004) showed that this law was able to explain (a) linear velocity profiles in plane shear flow and (b) Bagnold-like velocity profiles in chute flow. Jop, Forterre & Pouliquen (2005) showed how the function,  $\mu(I)$ , could be determined from the basal friction law measured by Pouliquen & Forterre (2002) and Jop, Forterre & Pouliquen (2006) converted the scalar rheology of GDR-MiDi (2004) into a full tensor constitutive law.

The  $\mu(I)$ -rheology has had a major impact on the field. Jop *et al.* (2006) used it to compute the steady downslope velocity down a pile constrained between rough side walls. The results agreed with experimental measurements of the free-surface velocity for a range of gap widths. Forterre (2006) performed a two-dimensional linear stability analysis of chute flow with the Bagnold velocity profile, and showed that the new rheology was able to predict the cutoff frequency, which matched the experiments of Forterre & Pouliquen (2003). More recently Lagrée, Staron & Popinet (2011) and Staron, Lagrée & Popinet (2012) have developed impressive two-dimensional time-dependent simulations for granular column collapses and silo flow. Barker *et al.* (2014) have shown that for a large intermediate range of the inertial number  $I$  the  $\mu(I)$ -rheology is well-posed, which lends considerable weight to the theory. However, they also show that for both high and low values of  $I$  the theory is ill-posed, i.e. grid-scale noise will grow without bound as the resolution tends to zero. Numerical results will therefore be grid dependent in the ill-posed region of parameter space, which is not desired. Ill-posedness sounds disastrous, but it is actually a very useful indication that some important physics is missing in the model. In this case it suggests that for very slow flows, shear bands (e.g. Wu, Bauer & Kolymbas 1996) and force chains become important (Majmudar & Behringer 2005), while rapid flows can transition to a granular gas where binary collisions dominate (e.g. Jenkins & Savage 1983; Goldhirsch 2003). In these regions of parameter space it is anticipated that other equations apply.

The success of the  $\mu(I)$ -rheology opens up the question as to whether it can be used to improve depth-averaged avalanche models, which are, for instance, unable to

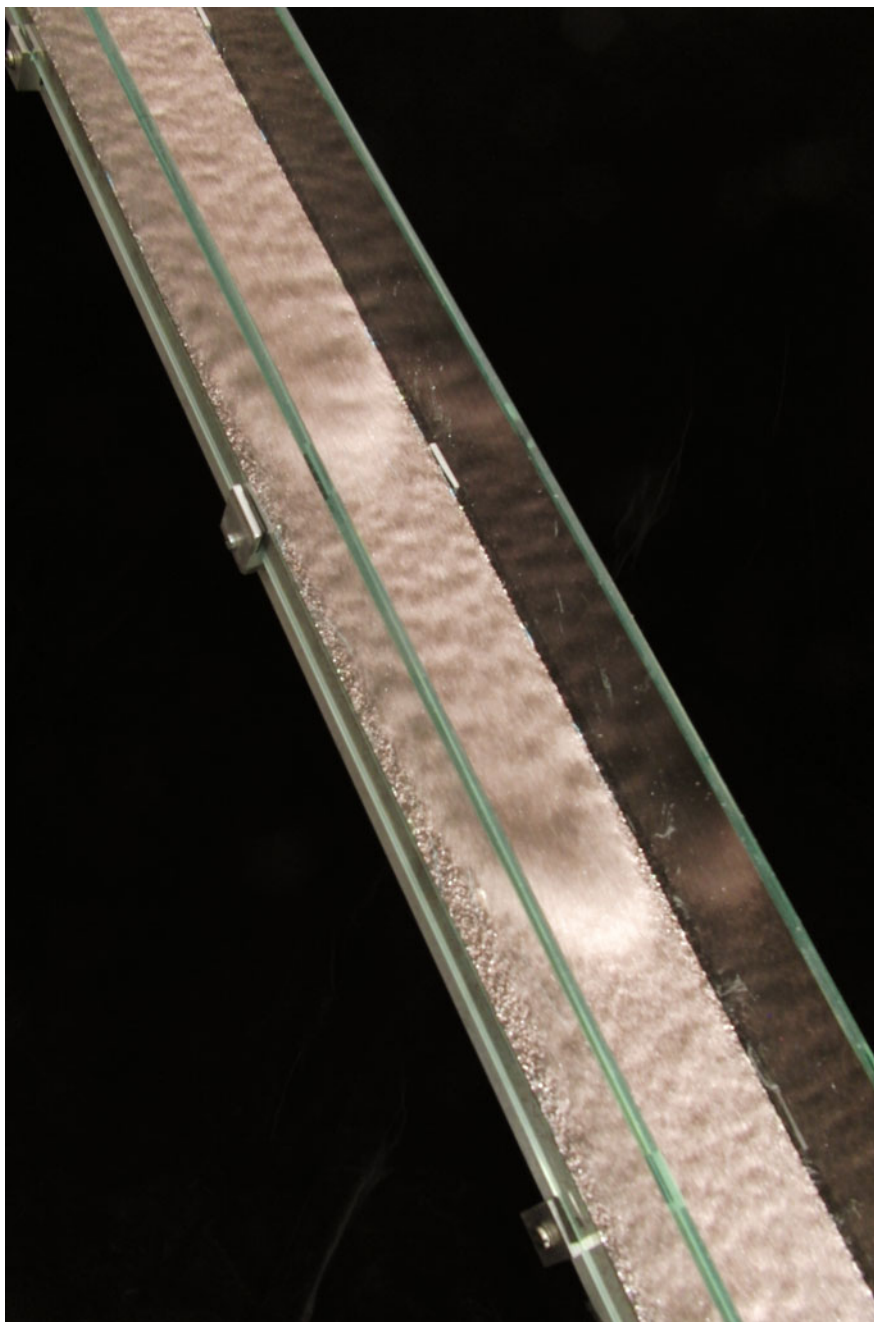


FIGURE 1. An oblique head-on view of a series of granular roll waves in an avalanche of 300–355  $\mu\text{m}$  carborundum particles flowing down a channel inclined at  $35.1^\circ$  to the horizontal. All of the grains are in motion, and two roll-wave crests can be seen that have a sharp brightly illuminated front and a shallower darker lee side.

predict the cutoff frequency of the roll-wave instability. Forterre (2006) has already thought along these lines. He used a heuristic argument to include the depth-averaged in-plane stress gradients in the downslope momentum balance, to generate a nonlinear

viscous term. While this was able to match the experimental cutoff frequency for the instability, an additional scaling factor had to be used. In addition, the viscosity had a singularity as the thickness tended to zero, which also is problematical. This paper therefore seeks to re-examine the approximations necessary in the depth-integration of the  $\mu(I)$ -rheology and come up with an improved formulation, that is able to predict the cutoff frequency of the roll-wave instability (Forterre & Pouliquen 2003) and might provide a rationally based regularization for coupled models of segregation-induced finger formation (see e.g. Woodhouse *et al.* 2012).

## 2. Governing equations and the $\mu(I)$ -rheology

Let  $Oxz$  be a rectangular Cartesian coordinate system with the  $x$ -axis orientated down a slope at an angle  $\zeta$  to the horizontal and the  $z$ -axis being the upward pointing normal. The velocity  $\mathbf{u}$  has components  $(u, w)$  in the  $(x, z)$  directions, respectively, and the grains have constant intrinsic density,  $\rho^*$ . The solids volume fraction,  $\Phi$ , is assumed to be constant and uniform throughout the material (GDR-MiDi 2004), so the partial density,  $\rho = \Phi\rho^*$ , is constant and uniform, and mass balance implies that the granular material is incompressible

$$\nabla \cdot \mathbf{u} = 0. \quad (2.1)$$

The momentum balance equation is

$$\rho \left( \frac{\partial \mathbf{u}}{\partial t} + \nabla \cdot (\mathbf{u} \otimes \mathbf{u}) \right) = \nabla \cdot \boldsymbol{\sigma} + \rho \mathbf{g}, \quad (2.2)$$

where  $t$  is time,  $\nabla$  is the gradient operator, ' $\cdot$ ' is the dot product,  $\otimes$  is the dyadic product,  $\boldsymbol{\sigma}$  is the Cauchy stress tensor and  $\mathbf{g}$  is the gravitational acceleration vector. The Cauchy stress is decomposed into an isotropic pressure  $p$  and a deviatoric stress  $\boldsymbol{\tau}$

$$\boldsymbol{\sigma} = -p\mathbf{1} + \boldsymbol{\tau}, \quad (2.3)$$

where  $\mathbf{1}$  is the unit tensor. The constitutive model for the granular material is provided by the  $\mu(I)$ -rheology (Jop *et al.* 2005, 2006), which is a nonlinear viscous law with a pressure- and strain-rate-dependent viscosity of the form

$$\boldsymbol{\tau} = \mu(I)p \frac{\mathbf{D}}{\|\mathbf{D}\|}, \quad (2.4)$$

where  $\mu$  is the friction law and  $I$  is the inertial number. The strain-rate  $\mathbf{D}$  is defined in terms of the velocity gradient  $\mathbf{L} = \nabla \mathbf{u}$  as

$$\mathbf{D} = \frac{1}{2} (\mathbf{L} + \mathbf{L}^T), \quad (2.5)$$

and  $\|\mathbf{D}\|$  is a second invariant of the strain-rate tensor

$$\|\mathbf{D}\| = \sqrt{\frac{1}{2} \text{tr } \mathbf{D}^2}, \quad (2.6)$$

where  $\text{tr}$  is the trace. Note that (2.5) is the standard definition of the strain-rate tensor, which differs from the definition used by Jop *et al.* (2006), so there is an extra factor of two in the definition of the non-dimensional inertial number

$$I = \frac{2\|\mathbf{D}\|d}{\sqrt{p/\rho^*}}, \quad (2.7)$$

$$\zeta_1 = 20.9^\circ \quad \zeta_2 = 32.76^\circ \quad \beta = 0.136 \quad \mathcal{L} = 0.825 \times 10^{-3} \text{ m}$$

TABLE 1. Rheological parameters measured by Forterre &amp; Pouliquen (2003).

where  $d$  is the diameter of the grains. The inertial number is the ratio of the time scale for microscopic rearrangements of the particles at a given confining pressure,  $d/\sqrt{p/\rho^*}$ , to the time scale given by the bulk shear rate,  $1/\|\mathbf{D}\|$ , and is equal to the square root of the Savage or Coulomb number (Savage 1984; Ancey, Coussot & Evesque 1999). Note that in the definition (2.7) the intrinsic solid density of the grains,  $\rho^*$ , is used rather than the partial density,  $\rho$ , which includes the interstitial pore space.

The rate dependence in the rheology (2.4) arises from the increase of the friction coefficient,  $\mu$ , with increasing inertial number,  $I$ . The dependence was determined from basal friction measurements that were made on an inclined plane (Pouliquen 1999a; Pouliquen & Forterre 2002). They observed that steady-uniform depth flows developed between two critical inclination angles  $\zeta_1$  and  $\zeta_2$ . For slope angles below  $\zeta_1$  there was no flow and for angles above  $\zeta_2$  the flows accelerated. In the steady-uniform regime they determined the empirical basal friction law

$$\mu(Fr, h) = \mu_1 + \frac{\mu_2 - \mu_1}{\frac{\beta h}{\mathcal{L} Fr} + 1}, \quad (2.8)$$

where the friction coefficients  $\mu_1 = \tan \zeta_1$  and  $\mu_2 = \tan \zeta_2$ . The parameter  $\beta$  is a dimensionless empirical constant (Pouliquen 1999a), whilst  $\mathcal{L}$  has the dimensions of a length and is characterized by the depth of flow over which a transition between the angles  $\zeta_1$  and  $\zeta_2$  occurs and, as such, is dependent on the material properties of the flowing particles and on the bed roughness conditions. The values of the rheological parameters used in this paper are those found by Forterre & Pouliquen (2003) and are given in table 1.

On an inclined plane the Froude number

$$Fr = \frac{\bar{u}}{\sqrt{gh \cos \zeta}}, \quad (2.9)$$

is defined as the ratio of the depth-averaged flow velocity,  $\bar{u}$ , to the gravity wave speed,  $\sqrt{gh \cos \zeta}$ , where  $g$  is the constant of gravitational acceleration and  $h$  is the flow thickness (see e.g. Gray *et al.* 2003). In these steady-uniform flows the inertial number,  $I$ , is constant and there is a Bagnold velocity profile through their depth (GDR-MiDi 2004). Using the fact that the depth-averaged Bagnold velocity is equal to

$$\bar{u} = \frac{2I}{5d} \sqrt{\Phi g \cos \zeta} h^{3/2}, \quad (2.10)$$

Jop *et al.* (2005) substituted for the Froude number and the depth-averaged velocity in (2.8) to obtain a general expression for the friction as a function of the inertial number

$$\mu(I) = \mu_1 + \frac{\mu_2 - \mu_1}{I_0/I + 1}, \quad (2.11)$$

where the constant

$$I_0 = \frac{5\beta d}{2\sqrt{\Phi} \mathcal{L}}. \quad (2.12)$$



The basal and internal friction laws are therefore intimately linked. The friction law (2.8) is only strictly valid for Froude numbers above  $\beta$ . For Froude numbers below this value, Pouliquen & Forterre (2002) determined a transition law, which plays an important role in the development of static regions (see e.g. Mangeney *et al.* 2007; Johnson & Gray 2011). Note, that the use of the Froude number (2.9) corrects for an angle dependence in  $I_0$  that was present in the original derivation of Jop *et al.* (2005) (in their appendix A).

The granular material is subject to kinematic conditions at its free surface and its base. These are formulated in terms of functions,  $F^s = z - s(x, t)$  and  $F^b = b(x, t) - z$ , which define outward pointing normals,  $\mathbf{n}^s = \nabla F^s / |\nabla F^s|$  and  $\mathbf{n}^b = \nabla F^b / |\nabla F^b|$ , at the surface and base, respectively. The functions,  $F^s$  and  $F^b$ , are identically zero at  $z = s(x, t)$  and  $z = b(x, t)$ , which implies the material derivatives are zero

$$\frac{\partial F^s}{\partial t} + \mathbf{u}^s \cdot \nabla F^s = 0, \quad z = s(x, t), \quad (2.13)$$

$$\frac{\partial F^b}{\partial t} + \mathbf{u}^b \cdot \nabla F^b = 0, \quad z = b(x, t), \quad (2.14)$$

where the superscripts ‘s’ and ‘b’ on the velocity indicate evaluation at the surface and base, respectively. In addition, the free-surface of the flow is assumed to be traction free and there is a no slip at the base

$$\boldsymbol{\sigma}^s \mathbf{n}^s = \mathbf{0}, \quad z = s(x, t), \quad (2.15)$$

$$\mathbf{u}^b = \mathbf{0}, \quad z = b(x, t). \quad (2.16)$$

The no slip condition is consistent with observations of flows on rough beds made of particles of the same size and shape that are glued to the base (Pouliquen 1999a,b; Pouliquen & Forterre 2002; GDR-MiDi 2004). This differs from the usual basal boundary condition imposed by Savage & Hutter (1989) and Gray *et al.* (1999) who assumed tangential slip with a Mohr–Coulomb friction law that was independent of the internal properties of the material.

### 3. Non-dimensionalization and depth-integration

#### 3.1. Scaling

The shallowness of the flow is now exploited in order to obtain simplified depth-averaged equations. The avalanche is assumed to be of a typical thickness,  $H$ , which is much smaller than the downslope length scale,  $L$ . Typical downstream flow speeds are assumed to be of the order of the gravity wave speed,  $U = (gH)^{1/2}$ , and mass balance implies that typical normal velocities in the  $z$  direction are of magnitude  $\varepsilon U$ , where the aspect ratio  $\varepsilon = H/L \ll 1$ . Note that this velocity scaling differs from that of Savage & Hutter (1989), who used the faster scale  $U = (gL)^{1/2}$ . The pressure scaling,  $\rho gH$ , is based on a lithostatic balance in the normal momentum equation. Typical magnitudes for the strain-rate and, hence, the deviatoric stresses can then be determined from the constitutive relations (2.4)–(2.6). This suggests introducing non-dimensional variables, indicated by the hat, of the form

$$\left. \begin{aligned} (x, z, s, b, h, d, \mathcal{L}) &= L(\hat{x}, \varepsilon \hat{z}, \varepsilon \hat{s}, \varepsilon \hat{b}, \varepsilon \hat{h}, \varepsilon \hat{d}, \varepsilon \hat{\mathcal{L}}), \quad t = L/\sqrt{gH} \hat{t}, \\ (u, w, \mathbf{u}, |\mathbf{u}|, \bar{u}) &= \sqrt{gH}(\hat{u}, \varepsilon \hat{w}, \hat{\mathbf{u}}, |\hat{\mathbf{u}}|, \hat{\bar{u}}), \\ (D_{xx}, D_{xz}, D_{zz}, \|\mathbf{D}\|) &= \sqrt{g/H}(\varepsilon \hat{D}_{xx}, \hat{D}_{xz}, \varepsilon \hat{D}_{zz}, \|\hat{\mathbf{D}}\|), \\ (p, \tau_{xx}, \tau_{xz}, \tau_{zz}, \boldsymbol{\sigma}) &= \rho gH(\hat{p}, \varepsilon \hat{\tau}_{xx}, \hat{\tau}_{xz}, \varepsilon \hat{\tau}_{zz}, \hat{\boldsymbol{\sigma}}). \end{aligned} \right\} \quad (3.1)$$

The non-dimensional mass balance equation and the downslope and normal components of the momentum balance are

$$\frac{\partial \hat{u}}{\partial \hat{x}} + \frac{\partial \hat{w}}{\partial \hat{z}} = 0 \quad (3.2)$$

$$\varepsilon \left( \frac{\partial \hat{u}}{\partial \hat{t}} + \frac{\partial}{\partial \hat{x}}(\hat{u}^2) + \frac{\partial}{\partial \hat{z}}(\hat{u}\hat{w}) \right) = -\varepsilon \frac{\partial \hat{p}}{\partial \hat{x}} + \varepsilon^2 \frac{\partial \hat{\tau}_{xx}}{\partial \hat{x}} + \frac{\partial \hat{\tau}_{xz}}{\partial \hat{z}} + \sin \zeta, \quad (3.3)$$

$$\varepsilon^2 \left( \frac{\partial \hat{w}}{\partial \hat{t}} + \frac{\partial}{\partial \hat{x}}(\hat{u}\hat{w}) + \frac{\partial}{\partial \hat{z}}(\hat{w}^2) \right) = -\frac{\partial \hat{p}}{\partial \hat{z}} + \varepsilon \frac{\partial \hat{\tau}_{xz}}{\partial \hat{x}} + \varepsilon \frac{\partial \hat{\tau}_{zz}}{\partial \hat{z}} - \cos \zeta, \quad (3.4)$$

which reveal the dominant balances in the equations. The surface and basal kinematic conditions (2.13) and (2.14) become

$$\frac{\partial \hat{s}}{\partial \hat{t}} + \hat{u} \frac{\partial \hat{s}}{\partial \hat{x}} - \hat{w} = 0, \quad \hat{z} = \hat{s}(\hat{x}, \hat{t}), \quad (3.5)$$

$$\frac{\partial \hat{b}}{\partial \hat{t}} + \hat{u} \frac{\partial \hat{b}}{\partial \hat{x}} - \hat{w} = 0, \quad \hat{z} = \hat{b}(\hat{x}, \hat{t}), \quad (3.6)$$

and the downslope and normal components of the surface traction (2.15) are

$$\varepsilon \hat{p} \frac{\partial \hat{s}}{\partial \hat{x}} - \varepsilon^2 \hat{\tau}_{xx} \frac{\partial \hat{s}}{\partial \hat{x}} + \hat{\tau}_{xz} = 0, \quad \hat{z} = \hat{s}(\hat{x}, \hat{t}), \quad (3.7)$$

$$-\varepsilon \hat{\tau}_{xz} \frac{\partial \hat{s}}{\partial \hat{x}} - \hat{p} + \varepsilon \hat{\tau}_{zz} = 0, \quad \hat{z} = \hat{s}(\hat{x}, \hat{t}). \quad (3.8)$$

### 3.2. Pressure, stress and velocity profiles with depth

To leading order in the small parameter,  $\varepsilon$ , the normal component of the momentum balance (3.4) and the surface traction condition (3.8) imply

$$\frac{\partial \hat{p}}{\partial \hat{z}} = -\cos \zeta, \quad \hat{p}(\hat{s}) = 0, \quad (3.9)$$

which can be integrated to show that the pressure is lithostatic

$$\hat{p} = (\hat{s} - \hat{z}) \cos \zeta. \quad (3.10)$$

The pressure at the base of the avalanche is

$$\hat{p}^b = (\hat{s} - \hat{b}) \cos \zeta = \hat{h} \cos \zeta, \quad (3.11)$$

where  $\hat{h} = \hat{s} - \hat{b}$  is the non-dimensional thickness, and the depth-averaged pressure

$$\hat{\bar{p}} = \frac{1}{\hat{h}} \int_{\hat{b}}^{\hat{s}} \hat{p} \, d\hat{z} = \frac{1}{2} \hat{h} \cos \zeta. \quad (3.12)$$

The leading-order momentum balance and surface traction conditions in the downslope direction, (3.3) and (3.7), reduce to

$$\frac{\partial \hat{\tau}_{xz}}{\partial \hat{z}} = -\sin \zeta, \quad \hat{\tau}_{xz}(\hat{s}) = 0, \quad (3.13a,b)$$



which implies that

$$\hat{\tau}_{xz} = (\hat{s} - \hat{z}) \sin \zeta. \quad (3.14)$$

Since the shear strain-rate and the second strain-rate invariant are equal to

$$\hat{D}_{xz} = \frac{1}{2} \frac{\partial \hat{u}}{\partial \hat{z}} + O(\varepsilon^2), \quad \|\hat{\mathbf{D}}\| = \frac{1}{2} \left| \frac{\partial \hat{u}}{\partial \hat{z}} \right| + O(\varepsilon), \quad (3.15a,b)$$

the deviatoric shear stress

$$\hat{\tau}_{xz} = \mu(I) \hat{p} \operatorname{sgn} \left( \frac{\partial \hat{u}}{\partial \hat{z}} \right), \quad (3.16)$$

where ‘sgn’ is the sign function. Using the lithostatic pressure relation (3.10) and assuming that the sign of  $\partial \hat{u} / \partial \hat{z}$  is positive, (3.14) can be equated to (3.16) to show that

$$\mu(I) = \tan \zeta. \quad (3.17)$$

From the definition of  $\mu(I)$ , in (2.11), it follows that the inertial number,  $I$ , is equal to the constant,  $I_\zeta$ , through the depth of the flow, where

$$I_\zeta = I_0 \left( \frac{\tan \zeta - \tan \zeta_1}{\tan \zeta_2 - \tan \zeta} \right), \quad (3.18)$$

is dependent on the inclination angle  $\zeta$ . As  $\zeta \rightarrow \zeta_1$ , the inertial number,  $I_\zeta \rightarrow 0$ , while as  $\zeta \rightarrow \zeta_2$ , the inertial number,  $I_\zeta \rightarrow \infty$ , so the whole range of  $I$  is realized by simply changing the slope angle,  $\zeta$ , from  $\zeta_1$  to  $\zeta_2$ . In non-dimensional variables the definition of the inertial number (2.7) becomes

$$I = \frac{2\|\hat{\mathbf{D}}\|\hat{d}}{\sqrt{\Phi}\hat{p}}. \quad (3.19)$$

Since  $I$  is equal to the constant  $I_\zeta$ , using (3.10) and (3.15), (3.19) reduces to an ordinary differential equation (ODE) for the velocity profile

$$\frac{\partial \hat{u}}{\partial \hat{z}} = \frac{I_\zeta \sqrt{\Phi \cos \zeta}}{\hat{d}} (\hat{s} - \hat{z})^{1/2}. \quad (3.20)$$

This can be integrated, subject to the no slip condition (2.16) at the base,  $\hat{u}(\hat{b}) = 0$ , to give a Bagnold-like velocity profile (e.g. GDR-MiDi 2004)

$$\hat{u} = \frac{2I_\zeta}{3\hat{d}} \sqrt{\Phi \cos \zeta} \left( \hat{h}^{3/2} - (\hat{s} - \hat{z})^{3/2} \right). \quad (3.21)$$

The depth-averaged Bagnold velocity is

$$\hat{\bar{u}} = \frac{1}{\hat{h}} \int_{\hat{b}}^{\hat{s}} \hat{u} \, d\hat{z} = \frac{2I_\zeta}{5\hat{d}} \sqrt{\Phi \cos \zeta} \hat{h}^{3/2}, \quad (3.22)$$

and hence the average of the square of the downslope velocity is

$$\overline{\hat{u}^2} = \frac{1}{\hat{h}} \int_{\hat{b}}^{\hat{s}} \hat{u}^2 \, d\hat{z} = \frac{5}{4} \hat{\bar{u}}^2. \quad (3.23)$$

## 3.3. Depth integration

The mass balance (3.2) and the downslope momentum balance (3.3) can now be integrated through the avalanche depth by using Leibniz' rule (Abramowitz & Stegun 1970) to exchange the order of differentiation and integration (see e.g. Gray *et al.* 1999; Gray & Kokelaar 2010a). The resulting equations can then be simplified by using the surface and basal kinematic conditions, (3.5) and (3.6), and the downslope surface traction condition (3.7) to give

$$\frac{\partial \hat{h}}{\partial \hat{t}} + \frac{\partial}{\partial \hat{x}}(\hat{h}\hat{u}) = 0, \quad (3.24)$$

$$\varepsilon \left( \frac{\partial}{\partial \hat{t}}(\hat{h}\hat{u}) + \frac{\partial}{\partial \hat{x}}(\hat{h}\hat{u}^2) + \frac{\partial}{\partial \hat{x}}(\hat{h}\hat{p}) \right) = \hat{h} \sin \zeta + |\nabla F^b| \mathbf{i} \cdot \hat{\boldsymbol{\sigma}}^b \mathbf{n}^b + \varepsilon^2 \frac{\partial}{\partial \hat{x}}(\hat{h}\hat{\tau}_{xx}), \quad (3.25)$$

where  $|\nabla F^b| = (1 + \varepsilon^2(\partial \hat{b}/\partial \hat{x})^2)^{1/2}$  and  $\mathbf{i}$  is the unit normal in the downslope direction. An expression is still needed for the downslope component of the basal traction. Instead of being able to substitute a traction condition, as in Savage & Hutter (1989), the internal Cauchy stress (2.3) must be evaluated at the base. Using the  $\mu(I)$ -rheology (2.4) and the basal pressure (3.11) it follows that

$$|\nabla F^b| \mathbf{i} \cdot \hat{\boldsymbol{\sigma}}^b \mathbf{n}^b = -\mu(I_\zeta) \hat{h} \cos \zeta \frac{\hat{D}_{xz}^b}{\|\hat{\mathbf{D}}^b\|} - \varepsilon \hat{h} \cos \zeta \frac{\partial \hat{b}}{\partial \hat{x}} + O(\varepsilon^2). \quad (3.26)$$

Since the no slip condition at the base (2.16) implies that  $\hat{u}(\hat{b})$  is identically zero, the  $xx$  component of the strain-rate at the base is zero, i.e.  $\hat{D}_{xx}^b = \partial \hat{u}/\partial \hat{x} = 0$ . The incompressibility relation (3.2) then implies that  $\hat{D}_{zz}^b = 0$ , since  $\partial \hat{w}/\partial \hat{z} = -\partial \hat{u}/\partial \hat{x} = 0$ , and hence  $\|\hat{\mathbf{D}}^b\| = |\hat{D}_{xz}^b|$  at the base. As a result the factor

$$\frac{\hat{D}_{xz}^b}{\|\hat{\mathbf{D}}^b\|} = \text{sgn}(\hat{D}_{xz}^b) = \text{sgn}(\hat{u}), \quad (3.27)$$

because (3.20) and (3.22) imply that the sign of  $\hat{D}_{xz}^b$  is the same as the sign of the depth-averaged velocity. In addition, following Jop *et al.* (2006), the friction coefficient can be expressed in terms of the Froude number and the flow thickness

$$\mu(I_\zeta) = \mu(Fr, \hat{h}), \quad (3.28)$$

as described in § 2. The traction condition (3.26) can therefore be expressed entirely in terms of depth-averaged variables.

Although the gravitational force,  $\hat{h} \sin \zeta$ , and the basal friction,  $\mu \hat{h} \cos \zeta$ , are both order-unity quantities, their difference, which arises in the source terms in (3.25), is typically much smaller. To formalize this, it is assumed that

$$\hat{h} \sin \zeta - \mu \hat{h} \cos \zeta \text{sgn}(\hat{u}) = \varepsilon \hat{h} \cos \zeta \left( \tan \zeta - \mu(Fr, \hat{h}) \text{sgn}(\hat{u}) \right) + O(\varepsilon^2), \quad (3.29)$$

i.e. gravity balances friction to leading order and their difference is small. The source terms are therefore of order  $\varepsilon$ , which allows the depth-averaged momentum balance (3.25) to be divided through by  $\varepsilon$ . When (3.26) and (3.29) are substituted

into (3.25), together with the approximations for the depth-averaged pressure (3.10) and the depth-averaged downslope velocity squared (3.23), the leading-order system of conservation laws becomes

$$\frac{\partial \hat{h}}{\partial \hat{t}} + \frac{\partial}{\partial \hat{x}}(\hat{h}\hat{u}) = 0, \quad (3.30)$$

$$\frac{\partial}{\partial \hat{t}}(\hat{h}\hat{u}) + \frac{\partial}{\partial \hat{x}}(\chi \hat{h}\hat{u}^2) + \frac{\partial}{\partial \hat{x}}\left(\frac{1}{2}\hat{h}^2 \cos \zeta\right) = \hat{h}\hat{S}, \quad (3.31)$$

where the shape factor  $\chi$  is the ratio of the depth-averaged square of the velocity,  $\overline{\hat{u}^2}$ , to the depth-averaged velocity squared,  $\hat{u}^2$ . Equation (3.23) implies that  $\chi$  is formally equal to 5/4 for the Bagnold velocity profile, but in virtually all granular flow models  $\chi$  is assumed to be unity for simplicity. Finally the source term

$$\hat{S} = \cos \zeta (\tan \zeta - \mu(Fr, \hat{h}) \operatorname{sgn}(\hat{u})) - \cos \zeta \frac{\partial \hat{b}}{\partial \hat{x}}, \quad (3.32)$$

is the combination of gravity acceleration, effective basal friction and topography gradients. Equations (3.30)–(3.32) are the familiar shallow-water-type avalanche equations, which are commonly used in the literature and have proved their effectiveness over many years (e.g. Grigorian *et al.* 1967; Savage & Hutter 1989; Gray *et al.* 1999; Pouliquen 1999b; Pouliquen & Forterre 2002; Gray *et al.* 2003). What is interesting is that the full shallow-water structure emerges naturally out of the leading-order balances, rather than having to include the depth-averaged pressure gradient and the basal topography gradients as order  $\varepsilon$  terms, as in Savage & Hutter (1989) and Gray *et al.* (2003). It is also interesting how the combination of the no slip condition (2.16) and the internal rheology (2.4) naturally give rise to an effective basal friction in the source terms (3.32). This is the only effect of the rheology on the flow, as the depth-averaged in-plane deviatoric stress gradient, which was present in (3.25), does not contribute to the leading-order momentum balance.

#### 4. Inclusion of depth-averaged viscous-like terms

Despite the effectiveness of the shallow-water-type avalanche models, higher-order terms are sometimes required to provide high-wavenumber cutoff of roll-wave instabilities (Forterre 2006) or to regularize models of segregation-induced fingering (Woodhouse *et al.* 2012). Trying to formally include all of the order- $\varepsilon$  effects is difficult and rapidly leads to theories that are too complex. A pragmatic approach is to simply include the in-plane deviatoric stress gradient, that was present in (3.25), because it will contain a second-order derivative in  $\bar{u}$ , which contributes to the principle part and introduces a singular perturbation to the problem. Let us therefore consider the modified downslope momentum balance

$$\frac{\partial}{\partial \hat{t}}(\hat{h}\hat{u}) + \frac{\partial}{\partial \hat{x}}(\chi \hat{h}\hat{u}^2) + \frac{\partial}{\partial \hat{x}}\left(\frac{1}{2}\hat{h}^2 \cos \zeta\right) = \hat{h}\hat{S} + \varepsilon \frac{\partial}{\partial \hat{x}}\left(\hat{h}\overline{\hat{\tau}_{xx}}\right), \quad (4.1)$$

and seek an approximation for the depth-averaged in-plane deviatoric stress using the approximations for the pressure (3.10), inertial number (3.17) and velocity profile (3.21) that have already been obtained in § 3.2. The  $\mu(I)$ -rheology (2.4) implies that

$$\hat{\tau}_{xx} = \mu(I)\hat{p}\frac{\hat{D}_{xx}}{\|\hat{\mathbf{D}}\|}. \quad (4.2)$$

Assuming  $\hat{h} = \hat{h}(\hat{x}, \hat{t})$  and  $\hat{s} = \hat{s}(\hat{x}, \hat{t})$ , the  $xx$ -component of the strain-rate tensor,  $\hat{\mathbf{D}}$ , can be calculated by differentiating the Bagnold velocity profile (3.21) with respect to  $\hat{x}$

$$\hat{D}_{xx} = \frac{\partial \hat{u}}{\partial \hat{x}} = \frac{I_\zeta \sqrt{\Phi \cos \zeta}}{\hat{d}} \left( \hat{h}^{1/2} \frac{\partial \hat{h}}{\partial \hat{x}} - (\hat{s} - \hat{z})^{1/2} \frac{\partial \hat{s}}{\partial \hat{x}} \right). \quad (4.3)$$

Provided  $\partial \hat{u} / \partial \hat{z}$  is positive, it follows from (3.15) and (3.20) that to leading order the second strain-rate invariant is

$$\|\hat{\mathbf{D}}\| = \frac{1}{2} \frac{\partial \hat{u}}{\partial \hat{z}} = \frac{I_\zeta \sqrt{\Phi \cos \zeta}}{2\hat{d}} (\hat{s} - \hat{z})^{1/2}. \quad (4.4)$$

Substituting (4.3) and (4.4) into (4.2), together with the expressions (3.10) and (3.17) for the lithostatic pressure and the inertial number, implies that

$$\hat{\tau}_{xx} = 2 \sin \zeta \left( \hat{h}^{1/2} (\hat{s} - \hat{z})^{1/2} \frac{\partial \hat{h}}{\partial \hat{x}} - (\hat{s} - \hat{z}) \frac{\partial \hat{s}}{\partial \hat{x}} \right). \quad (4.5)$$

Integrating this through the depth of the avalanche and eliminating the free-surface height, using  $\hat{s} = \hat{h} + \hat{b}$ , implies that

$$h \overline{\hat{\tau}_{xx}} = \int_{\hat{b}}^{\hat{s}} \hat{\tau}_{xx} d\hat{z} = \frac{1}{3} \hat{h}^2 \sin \zeta \frac{\partial \hat{h}}{\partial \hat{x}} - \hat{h}^2 \sin \zeta \frac{\partial \hat{b}}{\partial \hat{x}}. \quad (4.6)$$

This provides an approximation for the depth-averaged deviatoric in-plane stress arising in the momentum balance equation (4.1), but it is dependent on the gradient of the thickness,  $\partial \hat{h} / \partial \hat{x}$ , rather than having a dependence on the gradient of the depth-averaged velocity,  $\partial \hat{u} / \partial \hat{x}$ , as one might have expected. It can, however, be reformulated by using the depth-averaged Bagnold velocity (3.22) to substitute for the gradient

$$\frac{\partial \hat{h}}{\partial \hat{x}} = \frac{5\hat{d}}{3I_\zeta \sqrt{\Phi \cos \zeta}} \frac{1}{\hat{h}^{1/2}} \frac{\partial \hat{u}}{\partial \hat{x}}, \quad (4.7)$$

in (4.6) to give a depth-averaged nonlinear viscous law of the form

$$h \overline{\hat{\tau}_{xx}} = \hat{v} \hat{h}^{3/2} \frac{\partial \hat{u}}{\partial \hat{x}} - \hat{h}^2 \sin \zeta \frac{\partial \hat{b}}{\partial \hat{x}}, \quad (4.8)$$

where  $\hat{v} \hat{h}^{3/2} / 2$  is the coefficient of depth-averaged viscosity. The dependence on the thickness to the three halves power is a direct result of the  $\mu(I)$ -rheology. Note that the form of the viscous term is not unique, because the leading-order depth-averaged Bagnold velocity (3.22) could be used to obtain other formulations at this order. The form chosen in (4.8) has been specifically chosen because the coefficient does not have any singularities in the thickness  $\hat{h}$  or the depth-averaged velocity  $\hat{u}$ .

Using the definition of  $I_\zeta$ , in (3.18), and a non-dimensionalized version of the definition of  $I_0$ , (2.12), the coefficient  $\hat{v}$  can be expressed as

$$\hat{v} = \frac{5\hat{d} \sin \zeta}{9I_\zeta \sqrt{\Phi \cos \zeta}} = \frac{2\mathcal{L}}{9\beta} \frac{\sin \zeta}{\sqrt{\cos \zeta}} \left( \frac{\tan \zeta_2 - \tan \zeta}{\tan \zeta - \tan \zeta_1} \right). \quad (4.9)$$

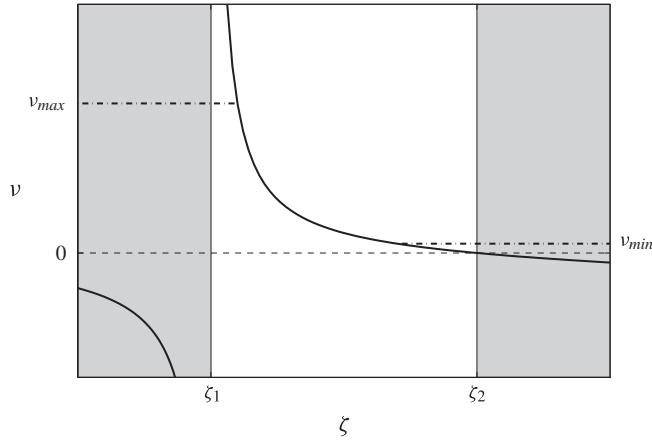


FIGURE 2. The coefficient  $\nu$  in the effective viscosity of the new depth-averaged  $\mu(I)$ -rheology is plotted as a function of the slope inclination angle  $\zeta$  (solid line). There is a singularity as  $\zeta \rightarrow \zeta_1$  and  $\nu$  becomes negative in the shaded region for  $\zeta < \zeta_1$ . At  $\zeta = \zeta_2$  the coefficient  $\nu = 0$  and becomes negative in the shaded region  $\zeta > \zeta_2$ . The effective viscosity will therefore be negative in these regions, which will lead to ill-posedness. By setting thresholds  $\nu_{min} \geq 0$  and  $\nu_{max} \geq 0$ , shown by the dot-dash lines, the depth-averaged rheology can be regularized for high and low inclination angles. However, this is not used in any of the results presented in the rest of this paper.

This has a very interesting dependence on the slope inclination angle,  $\zeta$ , for  $\zeta_1 \leq \zeta \leq \zeta_2$  as shown in figure 2. Avalanches on slopes with lower inclinations will experience a greater viscosity than if they are on higher-gradient slopes. In particular, as the slope inclination tends to the lower limit,  $\zeta \rightarrow \zeta_1$ , the viscosity,  $\hat{\nu} \rightarrow \infty$ . This could potentially play an important role in flow arrest processes. Conversely, as the slope inclination approaches the case of accelerated flow,  $\zeta \rightarrow \zeta_2$ , the viscosity tends to zero. For angles  $\zeta < \zeta_1$  and  $\zeta > \zeta_2$  the viscosity is negative. This sounds a note of caution, as problems with negative viscosities will be ill-posed. This may in part be because the leading-order steady-uniform flow assumptions in § 3.2 break down, but here it is also a signature of the underlying ill-posedness of the  $\mu(I)$ -rheology (Barker *et al.* 2014) at both high and low inertial numbers. For all of the problems treated in this paper  $\zeta \in [\zeta_1, \zeta_2]$ , so the theory is well-posed and no regularization is required or used. However, one may anticipate that readers will use the new depth-averaged theory to calculate the flow of an avalanche from its initiation on a steep slope to its run-out on a horizontal plane, which will require some form of regularization for both high and low inclination angles. A naive way of regularizing the depth-averaged theory would be to simply introduce non-negative maximum and minimum bounds for the viscosity, i.e.  $\nu \in [\nu_{min}, \nu_{max}] \geq 0$ , as shown by the dot-dash lines in figure 2. This would imply that the depth-averaged theory is mathematically well-posed for all slope angles, but whether this provides a useful theoretical fix remains untested.

The second term on the right-hand side of (4.8) arises from the interaction of the in-plane stresses with the prescribed topography,  $\hat{b}$ . It has the same  $\hat{h}^2$  thickness dependence as the depth-averaged pressure gradient term in (4.1), but is much smaller, being of order  $\varepsilon$ , and is therefore neglected. The first term in (4.8), however,

introduces a singular perturbation into the new system of conservation laws

$$\frac{\partial \hat{h}}{\partial \hat{t}} + \frac{\partial}{\partial \hat{x}}(\hat{h}\hat{u}) = 0, \quad (4.10)$$

$$\frac{\partial}{\partial \hat{t}}(\hat{h}\hat{u}) + \frac{\partial}{\partial \hat{x}}(\chi \hat{h}\hat{u}^2) + \frac{\partial}{\partial \hat{x}}\left(\frac{1}{2}\hat{h}^2 \cos \zeta\right) = \hat{h}\hat{S} + \varepsilon \frac{\partial}{\partial \hat{x}}\left(\hat{v}\hat{h}^{3/2} \frac{\partial \hat{u}}{\partial \hat{x}}\right), \quad (4.11)$$

since the highest-order gradient in (4.11) is multiplied by the small parameter  $\varepsilon$ . Equations (4.10) and (4.11) can be made dimensional again by applying the scalings

$$\left. \begin{aligned} x &= L\hat{x}, & (h, b, \mathcal{L}) &= H(\hat{h}, \hat{b}, \hat{\mathcal{L}}), & t &= L/\sqrt{gH}\hat{t}, \\ \bar{u} &= \sqrt{gH}\hat{u}, & S &= \varepsilon\hat{S}, & v &= \sqrt{gH}\hat{v}, \end{aligned} \right\} \quad (4.12)$$

to show that the depth-averaged mass and momentum balances are

$$\frac{\partial h}{\partial t} + \frac{\partial}{\partial x}(h\bar{u}) = 0, \quad (4.13)$$

$$\frac{\partial}{\partial t}(h\bar{u}) + \frac{\partial}{\partial x}(\chi h\bar{u}^2) + \frac{\partial}{\partial x}\left(\frac{1}{2}gh^2 \cos \zeta\right) = hgS + \frac{\partial}{\partial x}\left(vh^{3/2} \frac{\partial \bar{u}}{\partial x}\right), \quad (4.14)$$

where the dimensional source term is

$$S = \cos \zeta (\tan \zeta - \mu(Fr, h) \operatorname{sgn}(\bar{u})) - \cos \zeta \frac{\partial b}{\partial x}, \quad (4.15)$$

and the dimensional coefficient in the viscous law becomes

$$v = \frac{2}{9} \frac{\mathcal{L}\sqrt{g}}{\beta} \frac{\sin \zeta}{\sqrt{\cos \zeta}} \left( \frac{\tan \zeta_2 - \tan \zeta}{\tan \zeta - \tan \zeta_1} \right). \quad (4.16)$$

For the large majority of situations, the new depth-averaged  $\mu(I)$ -rheology can be neglected, but when sharp gradients in  $\bar{u}$  develop, a boundary-layer forms in which the viscous terms play a significant role. This system therefore has all the advantages of the classic shallow-water-type avalanche models (e.g. Grigorian *et al.* 1967; Savage & Hutter 1989; Gray *et al.* 1999; Pouliquen 1999b; Pouliquen & Forterre 2002; Gray *et al.* 2003), but has the extra physics necessary to obtain high-wavenumber cutoff (Forterre 2006) as well as the ability to regularize ill-posed models (Woodhouse *et al.* 2012).

## 5. Comparison with Forterre's depth-averaged $\mu(I)$ -rheology

Forterre (2006) used a heuristic approach to incorporate depth-averaged viscous stresses into the shallow-water-type avalanche equations. His argument was based on using (2.7) to rewrite the pressure,  $p$ , as a function of the inertial number as

$$p = 4 \frac{\rho^* d^2 \|\mathbf{D}\|^2}{I^2}, \quad (5.1)$$

and substituting it into (2.4) to obtain an expression for the in-plane deviatoric stress

$$\tau_{xx} = 2\rho^* d^2 \frac{\mu(I)}{I^2} \dot{\gamma} \frac{\partial u}{\partial x}, \quad (5.2)$$

where  $\dot{\gamma} = 2\|\mathbf{D}\|$ . In (5.2),  $\mu(I) = \tan \zeta$ , and  $I = I_\zeta$ , are constant at a given slope angle and are therefore independent of depth. In addition, Forterre (2006) assumed that  $\dot{\gamma}$  was also independent of depth and was then able to explicitly integrate (5.2) through the avalanche thickness to obtain

$$h\overline{\tau_{xx}} = \int_0^h \tau_{xx} dz = 2\rho^* d^2 \frac{\tan \zeta}{I_\zeta^2} \dot{\gamma} \frac{\partial}{\partial x} (h\bar{u}). \quad (5.3)$$

Forterre (2006) made the approximation that  $\dot{\gamma} = \bar{u}/(2h)$  in (5.3), but subsequently found that he needed to add an additional scaling factor,  $a$ , into the viscosity (in his momentum equations C2), which was set equal to 0.1, in order to get good agreement with the neutral stability curves for Forterre & Pouliquen's (2003) roll-wave experiments.

Using (5.3), it follows that Forterre's (2006) depth-averaged avalanche equations are

$$\frac{\partial h}{\partial t} + \frac{\partial}{\partial x} (h\bar{u}) = 0, \quad (5.4)$$

$$\frac{\partial}{\partial t} (h\bar{u}) + \frac{\partial}{\partial x} (\chi h\bar{u}^2) + \frac{\partial}{\partial x} \left( \frac{1}{2} h^2 g \cos \zeta \right) = hgS + \frac{\partial}{\partial x} \left( \nu_F \frac{\bar{u}}{h} \frac{\partial}{\partial x} (h\bar{u}) \right), \quad (5.5)$$

where the constant in the effective viscosity can be expressed as

$$\nu_F = ad^2 \frac{\tan \zeta}{I_\zeta^2 \Phi} = \frac{4a\mathcal{L}^2 \tan \zeta}{25\beta^2} \left( \frac{\tan \zeta_2 - \tan \zeta}{\tan \zeta - \tan \zeta_1} \right)^2, \quad (5.6)$$

by using (3.18) and (2.12). Note that just as in (4.16),  $\nu_F$  also has a singularity as  $\zeta \rightarrow \zeta_1$  and is equal to zero when  $\zeta = \zeta_2$ , but here it does not go negative. Equations (5.4) and (5.5) are identical to (4.13) and (4.14) except for the structure of the nonlinear viscous term, which is radically different. The new depth-averaged  $\mu(I)$ -rheology (4.14) has a viscous-like term with a gradient of the depth-averaged velocity,  $\partial \bar{u}/\partial x$ , multiplied by a coefficient of viscosity,  $\nu_F h^{3/2}/2$ , which is degenerate as  $h \rightarrow 0$ , i.e. the diffusion coefficient is zero when  $h = 0$ . Whereas Forterre's (2006) viscous-like term in (5.5) is based on gradients of the depth-averaged momentum,  $\partial(h\bar{u})/\partial x$ , and is multiplied by an effective viscosity  $\nu_F \bar{u}/(2h)$ , which is degenerate in  $\bar{u}$ , but is singular in  $h$ , i.e. the viscosity tends to infinity as  $h \rightarrow 0$ .

## 6. Effect of viscosity on the shape of a granular flow front

The difference between the two depth-averaged viscous-like terms is immediately apparent when one considers the problem of a granular flow front propagating down a rough inclined plane. Pouliquen (1999b) showed experimentally that the flow front moves at constant speed,  $u_F$ , and develops a well-defined shape. By changing to a front centred frame of coordinates defined by the change of variables

$$\xi = x - u_F t, \quad \tau = t, \quad (6.1a,b)$$

the steady-state mass balance equation (4.13) in the travelling frame becomes

$$\frac{d}{d\xi} (h(\bar{u} - u_F)) = 0. \quad (6.2)$$



Integrating this subject to the boundary condition that  $h=0$  at  $\xi=0$  implies that either

$$h=0 \quad \text{or} \quad \bar{u}=u_F. \quad (6.3a,b)$$

This allows a solution to be constructed with a front located at  $\xi=0$ , ahead of which is a grain-free region for  $\xi>0$ . Behind the front ( $\xi\leq 0$ ) the depth-averaged velocity,  $\bar{u}$ , is equal to the front speed,  $u_F$ , and the frontal shape is given by  $h=h(\xi)$ . Since  $\bar{u}$  is constant everywhere, there are no gradients in the depth-averaged velocity, and hence the new depth-averaged  $\mu(I)$ -rheology, derived in §4, does not induce any viscous stresses. Assuming that the shape factor,  $\chi$ , equals unity and the topography,  $b$ , is flat, the depth-averaged momentum balance equation (4.14) therefore simply reduces to the inviscid case, i.e.

$$\frac{dh}{d\xi} = \tan \zeta - \mu(Fr, h). \quad (6.4)$$

Far upstream the solution is assumed to tend toward a steady-uniform flow, in which  $h=h_0$  and  $\bar{u}=\bar{u}_0$ , and there is a balance between  $\tan \zeta$  and  $\mu(Fr_0, h_0)$ , where

$$Fr_0 = \frac{\bar{u}_0}{\sqrt{gh_0 \cos \zeta}}, \quad (6.5)$$

is the steady-uniform Froude number. Using the definition of the friction law (2.8) it follows that the depth-averaged steady-uniform velocity

$$\bar{u}_0 = \frac{\beta \sqrt{g \cos \zeta}}{\mathcal{L} \gamma} h_0^{3/2}, \quad (6.6)$$

where the parameter  $\gamma$  is defined as

$$\gamma = \frac{\tan \zeta_2 - \tan \zeta}{\tan \zeta - \tan \zeta_1} = \frac{\beta h_0}{\mathcal{L} Fr_0}. \quad (6.7)$$

Since the depth-averaged velocity is constant everywhere, it is determined by (6.6), which using (2.12), (3.18) and (4.12) is the dimensional equivalent of the depth-averaged Bagnold velocity (3.22). It is useful to non-dimensionalize the problem using the steady-uniform flow depth,  $h_0$ , and depth-averaged velocity,  $\bar{u}_0$ , by

$$(h, x, \xi) = h_0(\tilde{h}, \tilde{x}, \tilde{\xi}), \quad \bar{u} = \bar{u}_0 \tilde{u}, \quad t = (h_0/\bar{u}_0) \tilde{t}, \quad (6.8a-c)$$

where the tilded variables are non-dimensional. These scalings imply that the differential equation (6.4) with the friction law (2.8) becomes

$$\frac{dh}{d\xi} = (\tan \zeta_2 - \tan \zeta_1) \left( \frac{1}{1 + \gamma} - \frac{1}{1 + \gamma h^{3/2}} \right), \quad (6.9)$$

where the tildes are now dropped for simplicity. Gray & Ancey (2009) showed that this could be integrated exactly to give  $\xi=\xi(h)$ . Pouliquen (1999b) numerically solved an equivalent version of this equation for the exponential form of the basal friction law (Pouliquen 1999a). The exact solution for the new depth-averaged rheology is shown by the dashed line in figure 3, for parameters  $\zeta_1 = 20.9^\circ$ ,  $\zeta = 29^\circ$ ,  $\zeta_2 = 32.76^\circ$ . The key point is that, for the front problem, the new depth-averaged  $\mu(I)$ -rheology gives the identical solution to the inviscid case. The results therefore not only automatically

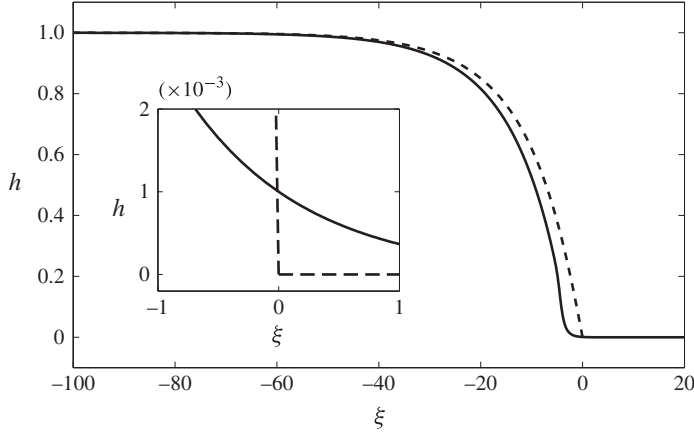


FIGURE 3. Comparison between the non-dimensional front thickness  $h$  for the new depth-averaged viscous model (dashed line) and Forterre's (2006) depth-averaged viscous model (solid line) in the moving coordinate  $\xi$  and for parameters  $\zeta_1 = 20.9^\circ$ ,  $\zeta = 29^\circ$  and  $\zeta_2 = 32.76^\circ$ . The new model has exactly the same solution as the inviscid case (Pouliquen 1999b; Gray & Ancey 2009) with a well-defined front and a grain-free region for  $\xi > 0$ . Conversely Forterre's (2006) model does not allow grain-free regions, as the inset diagram shows, and the shape of the front is sensitively dependent on the precise way in which  $h \rightarrow 0$  as  $\xi \rightarrow \infty$ . In the case illustrated here the exponential solution  $\epsilon \exp(r\xi)$ , for  $\xi > 0$  with  $r = -1$  and  $\epsilon = 10^{-3}$ , is matched to a numerical solution for  $Fr_0 = 1.02$  and  $R_F = 113.18$ , in the region  $\xi < 0$ , at  $\xi = 0$ .

match Pouliquen's (1999b) experimental data, but also naturally produce a completely grain-free region ahead of the front.

Conversely, the front problem for Forterre's (2006) depth-averaged rheology is affected by the viscous term. Even though mass balance still implies that if  $h = 0$  at the front, then  $\bar{u} = u_F$  everywhere, the viscous term involves the gradient of  $h\bar{u}$ , which is not constant. Assuming that far upstream there is steady-uniform flow, then  $\bar{u}$  is equal to the steady-uniform velocity,  $\bar{u}_0$ , everywhere. It follows that for shape factor  $\chi = 1$  and flat basal topography, the scalings (6.8) imply the non-dimensional depth-averaged momentum balance (5.5) in the moving frame is

$$h \frac{dh}{d\xi} = h(\tan \zeta_2 - \tan \zeta_1) \left( \frac{1}{1 + \gamma} - \frac{1}{1 + \gamma h^{3/2}} \right) + \frac{Fr_0^2}{R_F} \frac{d}{d\xi} \left( \frac{1}{h} \frac{dh}{d\xi} \right), \quad (6.10)$$

where the equivalent of the Reynolds number for this rheology is

$$R_F = \frac{h_0^2}{\nu_F}. \quad (6.11)$$

The last term on the right-hand side of (6.10) is the viscous term, and has a singularity in the viscosity as  $h \rightarrow 0$ , which is problematic at the flow front. To study the effect of this term, an expansion is made about  $h = 0$  by the introduction of a rescaled order unity thickness,  $\mathcal{H}$ , that satisfies

$$h = \epsilon \mathcal{H}, \quad \text{where } \epsilon \ll 1. \quad (6.12)$$

Substituting this into the differential equation (6.10) implies that to leading order in  $\epsilon$

$$\frac{d}{d\xi} \left( \frac{1}{\mathcal{H}} \frac{d\mathcal{H}}{d\xi} \right) = 0, \quad (6.13)$$

which can be integrated twice to show that

$$\mathcal{H} = qe^{r\xi}, \quad (6.14)$$

where  $q$  and  $r$  are constants of integration. Since the exponential function is strictly positive for finite  $\xi$ , the boundary condition  $\mathcal{H} = 0$  at  $\xi = 0$  can only be satisfied if  $q = 0$ , and hence  $\mathcal{H} = 0$  everywhere, which is not desired.

Non-trivial solutions can be constructed to Forterre's (2006) model for  $r < 0$ , but they only satisfy the boundary condition  $h = 0$  in the limit as  $\xi \rightarrow \infty$ . An example of such a solution is shown by the solid line in figure 3, for the same parameters as the inviscid case and with  $Fr_0 = 1.02$  and  $R_F = 113.18$ . The asymptotic solution (6.14) is used in  $\xi > 0$ , with parameters  $q = 1$ ,  $r = -1$  and  $\epsilon = 10^{-3}$ . It is matched onto a numerical solution by applying the initial conditions

$$h = \epsilon, \quad \frac{dh}{d\xi} = -\epsilon, \quad \text{at } \xi = 0, \quad (6.15)$$

and then integrating (6.10) for  $h$  in  $\xi < 0$ . Overall the solution lies close to the new depth-averaged result, which is indicated by the dashed line. However, as the inset image shows, Forterre's (2006) depth-averaged viscous term prevents the development of grain-free regions, and fills the whole domain with a thin layer of material. Since this very thin layer will be far below the actual grain size of the particles, one might argue that this is an irrelevance that could be ignored. In this case it is not, since it is possible to construct different solutions for other values of  $r$  and  $\epsilon$ . The front shape in Forterre's (2006) model is therefore sensitively dependent on the precise thickness of the precursor layer and the way in which it tends to zero as  $\xi \rightarrow \infty$ , which is not physically realistic. The new depth-averaged model (4.13)–(4.16), on the other hand, generates frontal shapes that agree with the experimental profiles measured by Pouliquen (1999b), and which are totally unaffected by the grain-free region.

## 7. Instability of steady-uniform flows

### 7.1. Non-dimensional steady-uniform flow equations

The new model (4.13)–(4.16) is non-dimensionalized about the steady-uniform flow thickness,  $h_0$ , and depth-averaged velocity,  $\bar{u}_0$ , using the scalings (6.8). Assuming the shape factor,  $\chi$ , equals unity and the basal topography,  $b$ , is flat, the non-dimensional depth-averaged mass and momentum balances become

$$\frac{\partial h}{\partial t} + \frac{\partial}{\partial x} (h\bar{u}) = 0, \quad (7.1)$$

$$F^2 h \left( \frac{\partial \bar{u}}{\partial t} + \bar{u} \frac{\partial \bar{u}}{\partial x} \right) + h \frac{\partial h}{\partial x} = h(\tan \zeta - \mu) + \frac{F^2}{R} \frac{\partial}{\partial x} \left( h^{3/2} \frac{\partial \bar{u}}{\partial x} \right), \quad (7.2)$$

where mass balance has been used to reduce the acceleration terms. The friction coefficient (2.8) can be written as

$$\mu(h, \bar{u}) = \tan \zeta_1 + \frac{\tan \zeta_2 - \tan \zeta_1}{1 + \gamma h^{3/2} / \bar{u}}, \quad (7.3)$$

where  $\gamma$  is defined in (6.7), and the Reynolds number,  $R$ , for the new rheology is defined in terms of the dimensional quantities as

$$R = \frac{\bar{u}_0 \sqrt{h_0}}{\nu}. \quad (7.4)$$

For notational simplicity the steady-uniform Froude number is denoted by

$$F = Fr_0, \quad (7.5)$$

which is defined by (6.5). It is convenient to use  $F$  as a parameter in the theory, which then sets the dimensional thickness,  $h_0$ , and dimensional velocity,  $\bar{u}_0$ , as well as the Reynolds number,  $R$ , by solving (6.7), (6.6) and (7.4), respectively.

### 7.2. Linear stability analysis

To study the linear stability of the steady-uniform flow, small perturbations are made about the base state  $h = 1$ ,  $\bar{u} = 1$  with the introduction of new variables

$$h = 1 + \epsilon \mathcal{H}, \quad \bar{u} = 1 + \epsilon \mathcal{U}, \quad \epsilon \ll 1. \quad (7.6a,b)$$

Substitution of the variables (7.6) into the non-dimensional system of equations (7.1) and (7.2) and collecting terms in orders of  $\epsilon$  shows that the  $O(1)$  equations are trivially satisfied, whilst the  $O(\epsilon)$  equations are

$$\frac{\partial \mathcal{H}}{\partial t} + \frac{\partial \mathcal{H}}{\partial x} + \frac{\partial \mathcal{U}}{\partial x} = 0, \quad (7.7)$$

$$F^2 \left( \frac{\partial \mathcal{U}}{\partial t} + \frac{\partial \mathcal{U}}{\partial x} \right) + \frac{\partial \mathcal{H}}{\partial x} = \Gamma \left( \frac{3}{2} \mathcal{H} - \mathcal{U} \right) + \frac{F^2}{R} \frac{\partial^2 \mathcal{U}}{\partial x^2}, \quad (7.8)$$

where the constant  $\Gamma$  is defined as

$$\Gamma = \frac{\gamma(\tan \zeta_2 - \tan \zeta_1)}{(1 + \gamma)^2}. \quad (7.9)$$

Solutions to the linearized equations (7.7) and (7.8) are sought in the form

$$(\mathcal{H}, \mathcal{U}) = (V_1, V_2) e^{i(kx - \omega t)} = (V_1, V_2) e^{-k_i x} e^{i(k_r x - \omega t)}, \quad (7.10)$$

for a complex wavenumber,  $k = k_r + ik_i$ , and real pulsation,  $\omega$ . This form is used because (Forterre & Pouliquen 2003) initiated the perturbations to their flow by using sound waves with a given pulsation frequency at a fixed location near the top of the chute. The spatial growth rate can therefore be defined as

$$\sigma = -\text{Im}(k) = -k_i, \quad (7.11)$$

and the phase velocity as

$$c = \frac{\omega}{\text{Re}(k)} = \frac{\omega}{k_r}. \quad (7.12)$$

Substituting for  $\mathcal{H}$  and  $\mathcal{U}$  using (7.10) reduces the linear stability equations to

$$\mathbf{A} \mathbf{V} = \mathbf{0}, \quad (7.13)$$

$$\zeta = 29.0^\circ \quad \gamma \approx 0.517 \quad \nu \approx 1.13 \times 10^{-3} \text{ m}^{3/2} \text{ s}^{-1} \quad F = 1.02 \quad R \approx 8.45$$

TABLE 2. Parameters for the new depth-averaged rheology corresponding to the conditions in Forterre & Pouliquen's (2003) experiments, shown in their figure 11.

where  $\mathbf{V} = (V_1, V_2)^T$ ,  $\mathbf{0} = (0, 0)^T$  and the matrix of coefficients is

$$\mathbf{A} = \begin{pmatrix} k - \omega & k \\ ik - \frac{3}{2}\Gamma & \Gamma + iF^2(k - \omega) + \frac{F^2k^2}{R} \end{pmatrix}. \quad (7.14)$$

For non-trivial solutions, the determinant,  $\det \mathbf{A} = 0$ , yields the dispersion relation

$$k^3 + \left( iR - \frac{iR}{F^2} - \omega \right) k^2 + R \left( \frac{5\Gamma}{2F^2} - 2i\omega \right) k + R \left( i\omega - \frac{\Gamma}{F^2} \right) \omega = 0. \quad (7.15)$$

This has one distinct complex root and a pair of complex conjugate roots. Explicit solutions for these three roots may be obtained by Cardano's solution to a cubic equation with complex coefficients. Of the three solution branches, only one has any region of positive spatial growth rate,  $\sigma$ , with a positive phase velocity (one solution always has negative growth with a positive phase velocity, the other always shows positive growth with a negative phase velocity, both implying spatial decay). Note that this implicitly assumes  $R$  is positive. If  $R$  is negative one the roots grows without bound, which implies that the equations are ill-posed if the coefficient in the viscosity,  $\nu$ , is negative.

The spatial growth rate and phase velocity for this solution branch are shown in figure 4 (solid lines), which are in good quantitative agreement with the experimental measurements (markers) made by Forterre & Pouliquen (2003). The parameter values for Forterre & Pouliquen's (2003) experiments and the implied values of  $\nu$  and  $R$  are summarized in table 2. Note that there are no adjustable parameters used in this comparison. In particular, the new-depth-averaged  $\mu(I)$ -rheology is able to predict a cutoff frequency,  $\omega_c$ , that is close to the experimental value, and similar to the results of Forterre's (2006) stability analysis using the full  $\mu(I)$ -rheology. This is a significant improvement on Forterre's (2006) depth-averaged rheology, which was only able to match the results by including the scaling factor,  $a$ , in the viscosity,  $\nu_F$ . It should be noted that in the absence of rheology, the classical granular avalanche equations (3.30)–(3.32) do not predict a cutoff frequency (Forterre & Pouliquen 2003), and instead the growth rate tends to a positive constant as the frequency tends to infinity, so the presence of a viscous term is vital to match experiments.

### 7.3. Cutoff frequency for instability using the new depth-averaged rheology

The cutoff frequency,  $\omega_c$ , is the frequency at which the growth rate is zero, that is  $\sigma = -k_i = 0$ , and the corresponding wavenumber has a critical value  $k_c = k_{r_c} \in \mathbb{R}$ . An expression for  $\omega_c$  is found by taking real and imaginary parts of the dispersion relation (7.15) with  $k = k_c$ , to give

$$\frac{F^2}{R}k_c^3 - \frac{F^2}{R}\omega_c k_c^2 + \frac{5\Gamma}{2}k_c - \Gamma\omega_c = 0, \quad (7.16)$$

$$(F^2 - 1)k_c^2 - 2F^2\omega_c k_c + F^2\omega_c^2 = 0, \quad (7.17)$$

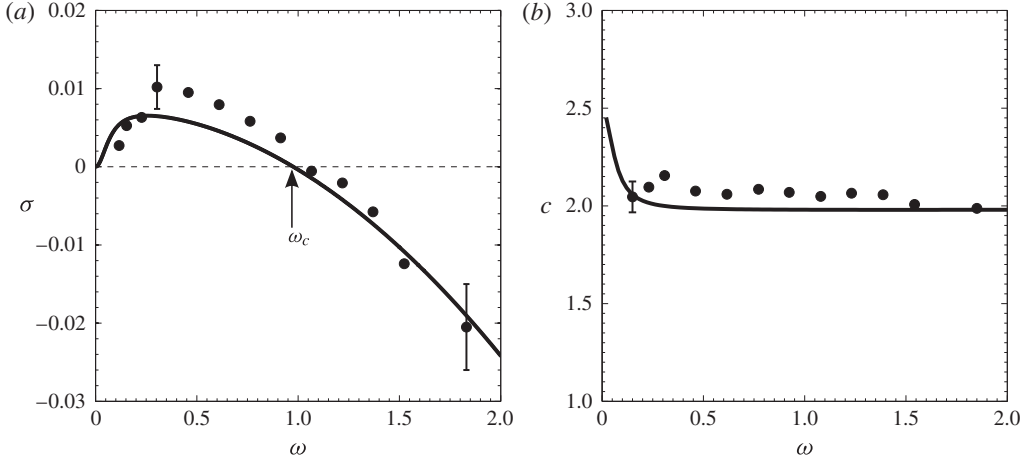


FIGURE 4. Comparison between the model using the new depth-averaged  $\mu(I)$ -rheology (solid lines) and the experimental results (symbols) of Forterre & Pouliquen (2003) for (a) the spatial growth rate  $\sigma$ , (b) the phase velocity  $c$ , as functions of the dimensionless frequency  $\omega$ , for  $\zeta = 29^\circ$  and  $F = 1.02$ . The cutoff frequency  $\omega_c$  is the frequency at which the growth rate of the instability is zero. All quantities are dimensionless, with the experimental data made so using the measured mean velocity and thickness at each point. Note that there are no adjustable parameters used in this comparison.

respectively. Solving the second of these gives a pair of quadratic roots for the critical wavenumber

$$k_{c\pm} = \frac{F}{F \mp 1} \omega_c. \quad (7.18)$$

Substitution of the roots (7.18) into (7.16) gives a quadratic for  $\omega_c$ ,

$$\pm \frac{F^4}{R(F \mp 1)^3} \omega_c^2 + \frac{5\Gamma F}{2(F \mp 1)} - \Gamma = 0, \quad (7.19)$$

(assuming  $\omega_c \neq 0$ ), which implies

$$\omega_c^2 = \mp \frac{(F \mp 1)^2}{F^4} R\Gamma \left( \frac{3F}{2} \pm 1 \right). \quad (7.20)$$

This has four distinct, non-trivial solutions for  $\omega_c$  given by

$$\omega_{c1\pm} = \frac{(F \mp 1)}{F^2} \sqrt{\mp R\Gamma \left( \frac{3}{2}F \pm 1 \right)}, \quad \omega_{c2\pm} = -\frac{(F \mp 1)}{F^2} \sqrt{\mp R\Gamma \left( \frac{3}{2}F \pm 1 \right)}. \quad (7.21a,b)$$

Two of the solutions  $\omega_{c1,2+}$  can immediately be discarded, since they are purely imaginary (with  $\Gamma, R, F > 0$ ) and the frequency  $\omega$  was assumed real. Next  $\omega_{c2-}$  is ignored since any non-zero real part is always negative. This leaves only one solution with positive real part for the cutoff frequency

$$\omega_c = \omega_{c1-} = \frac{(F+1)}{F^2} \sqrt{R\Gamma \left( \frac{3}{2}F - 1 \right)}, \quad (7.22)$$

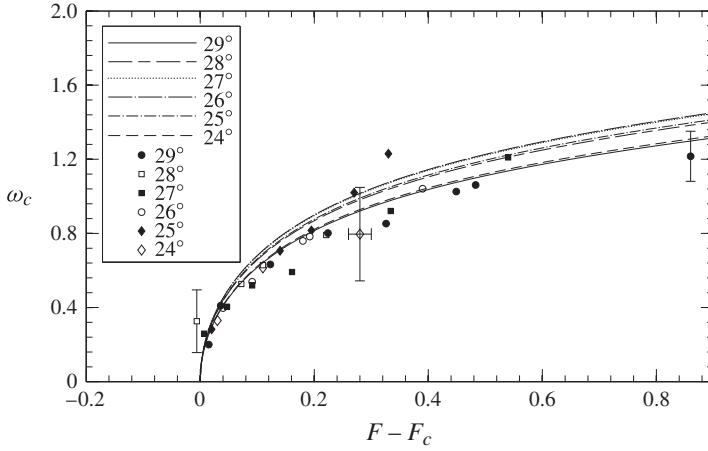


FIGURE 5. Comparison between the model using the new depth-averaged  $\mu(I)$ -rheology (lines) and experimental data (symbols) of Forterre & Pouliquen (2003) on the cutoff frequency,  $\omega_c$ , as a function of the Froude number  $F$  above the critical Froude number  $F_c = 2/3$  for a range of slope angles  $24^\circ \leq \zeta \leq 29^\circ$ . All quantities are dimensionless, with the experimental data made so using the measured mean velocity and thickness at each point. Note that there are no adjustable parameters used in this comparison.

which is purely real for  $F$  greater than the critical Froude number for the instability

$$F > F_c = \frac{2}{3}. \quad (7.23)$$

The real part of  $\omega_c$  is plotted as a function of  $F - F_c$  in figure 5 to give the neutral stability curves for integer values of the slope inclination angle  $\zeta$  between  $24^\circ$  and  $29^\circ$ . New values of  $R$  and  $\Gamma$  (along with all of the constituent parameters) must be calculated from the definitions (7.4) and (7.9), respectively, for each inclination. There is very good qualitative and quantitative agreement between the cutoff frequency predicted by the new depth-averaged  $\mu(I)$ -rheology (lines), with no fitting parameters, and that of the experimental data measured by Forterre & Pouliquen (2003) (markers). Quite surprisingly the new model is in better agreement with the experimental data than the cutoff frequency predicted using the full two-dimensional  $\mu(I)$ -rheology (Forterre 2006). It is also an improvement on Forterre's (2006) depth-averaged rheology, which needed an arbitrary fitting parameter. The near collapse of all of the neutral stability curves for different slope inclination angles is a direct result of the  $\zeta$  dependence in the coefficient  $\nu$  in the new depth-averaged  $\mu(I)$ -rheology, given by (4.16).

## 8. Granular roll waves with the new depth-averaged $\mu(I)$ -rheology

It is interesting to construct some solutions for the shape of granular roll waves, to see the effect of the new depth-averaged  $\mu(I)$ -rheology. In order to do this, it is convenient to switch to a coordinate system that moves at the same speed,  $u_w$ , as the roll wave, by making the coordinate transformation

$$\xi = x - u_w t, \quad \tau = t, \quad (8.1)$$



and then looking for steady-state solutions in the travelling frame to the non-dimensional system of conservations laws (7.1) and (7.2), which become

$$\frac{d}{d\xi}(h(\bar{u} - u_w)) = 0, \quad (8.2)$$

$$F^2 h(\bar{u} - u_w) \frac{d\bar{u}}{d\xi} + h \frac{dh}{d\xi} = h(\tan \zeta - \mu) + \frac{F^2}{R} \frac{d}{d\xi} \left( h^{3/2} \frac{d\bar{u}}{d\xi} \right). \quad (8.3)$$

The first of these can be integrated to show that,  $h(\bar{u} - u_w)$ , is constant. Since steady-uniform flow, in which  $h = 1$  and  $\bar{u} = 1$ , must be a solution of these equations, it follows that the constant equals,  $1 - u_w$ , and hence that

$$\bar{u} = u_w + \frac{1 - u_w}{h}. \quad (8.4)$$

Substituting (8.4) into the momentum balance (8.3) leads to the second-order ODE for  $h(\xi)$ , that governs roll-wave solutions,

$$\frac{d^2 h}{d\xi^2} = \frac{1}{2h} \left( \frac{dh}{d\xi} \right)^2 + \frac{Rh^{3/2}}{F^2(u_w - 1)} \left[ \left( 1 - \frac{F^2(u_w - 1)^2}{h^3} \right) \frac{dh}{d\xi} - \tan \zeta + \mu(h) \right], \quad (8.5)$$

where the friction  $\mu$  is expressed as a function of  $h$  (only) as

$$\mu(h) = \tan \zeta_1 + \frac{(\tan \zeta_2 - \tan \zeta_1)(1 - u_w + u_w h)}{1 - u_w + u_w h + \gamma h^{5/2}}. \quad (8.6)$$

It is convenient to write the second-order ODE (8.5) as a system of first-order phase-plane equations in order to study the existence of limit cycles. Defining

$$\frac{dh}{d\xi} = n, \quad (8.7)$$

and substituting this into (8.5) gives

$$\frac{dn}{d\xi} = \frac{n^2}{2h} + \frac{Rh^{3/2}}{F^2(u_w - 1)} \left[ \left( 1 - \frac{F^2(u_w - 1)^2}{h^3} \right) n - \tan \zeta + \mu(h) \right]. \quad (8.8)$$

The first-order system of ODEs (8.7) and (8.8) has an equilibrium, or fixed point, at  $(h, n) = (1, 0)$ . For a given value of the steady-uniform Froude number,  $F$ , and the Reynolds number,  $R$ , (8.7) and (8.8) can be solved for  $(h, n)$  with the speed of the wave,  $u_w$ , acting as a control parameter.

### 8.1. The existence of stable limit cycles

Before numerically solving (8.7) and (8.8) to find periodic roll-wave solutions, it is useful to constrain the values of  $u_w$  for which closed periodic orbits in phase space exist. The existence and classification of limit cycles in the phase-plane equations (8.7) and (8.8) is determined by a linearization in the neighbourhood of the fixed point  $(1, 0)$  (e.g. Needham & Merkin 1984; Jordan & Smith 1987; Strogatz 1994). Expanding about this point with

$$h = 1 + \epsilon \mathcal{H}, \quad n = \epsilon \mathcal{N}, \quad \epsilon \ll 1, \quad (8.9a,b)$$

the  $O(1)$  equations are trivially satisfied, whilst the  $O(\epsilon)$  terms give the linear system

$$\frac{d\mathcal{H}}{d\xi} = \mathbf{B}\mathcal{H}, \quad (8.10)$$

where  $\mathcal{H} = (\mathcal{H}, \mathcal{N})^T$  and the matrix of coefficients is

$$\mathbf{B} = \begin{pmatrix} 0 & 1 \\ \frac{R\Gamma(2u_w - 5)}{2F^2(u_w - 1)} & \frac{R[1 - F^2(u_w - 1)^2]}{F^2(u_w - 1)} \end{pmatrix}. \quad (8.11)$$

The eigenvalues,  $\lambda$ , which classify the equilibrium point are found by solving

$$\det(\mathbf{B} - \lambda \mathbf{I}) = 0, \quad (8.12)$$

where  $\mathbf{I}$  is the identity matrix. This yields the quadratic equation

$$\lambda^2 - \frac{R[1 - F^2(u_w - 1)^2]}{F^2(u_w - 1)}\lambda - \frac{\Gamma R(2u_w - 5)}{2F^2(u_w - 1)} = 0 \quad (8.13)$$

which has roots

$$\lambda_{1,2} = \frac{R[1 - F^2(u_w - 1)^2]}{2F^2(u_w - 1)} \left(1 \pm \sqrt{\Delta}\right), \quad (8.14)$$

where the discriminant

$$\Delta = 1 + \frac{2\Gamma F^2(u_w - 1)(2u_w - 5)}{R[1 - F^2(u_w - 1)^2]^2}. \quad (8.15)$$

Considering the wavespeed  $u_w$  as the bifurcation parameter, the behaviour of the equilibrium point is considered for all values of  $u_w > 0$ . First, for  $u_w < 1$  and  $u_w \geq 5/2$  the discriminant  $\Delta \geq 1$ , hence the eigenvalues  $\lambda_{1,2}$  are always real and of opposite sign, which implies that the equilibrium point is a saddle and there can be no limit cycles surrounding it. Next, in the special case  $u_w = 1$ , the linear system (8.10) and (8.11) is singular. Returning to depth-averaged velocity relation (8.4) with  $u_w = 1$  implies that  $\bar{u} = u_w = 1$  everywhere, and so the first-order ODE (6.9) for the front problem is recovered. In this case it is already known that there can be no limit cycles surrounding the equilibrium. Finally, for  $1 < u_w < 5/2$ , the discriminant  $\Delta < 0$  provided

$$\frac{2\Gamma F^2(u_w - 1)(5 - 2u_w)}{R[1 - F^2(u_w - 1)^2]^2} > 1, \quad (8.16)$$

in which case the eigenvalues  $\lambda_{1,2}$  are complex conjugates and there is a spiral which will be unstable or stable dependent on whether the real part

$$\text{Re}\{\lambda_{1,2}\} = \frac{R[1 - F^2(u_w - 1)^2]}{2F^2(u_w - 1)}, \quad (8.17)$$

is positive or negative. The real part is zero at the bifurcation point

$$u_w = u_c = 1 + \frac{1}{F}. \quad (8.18)$$

Since the above is true only for  $1 < u_w < 5/2$ , it follows that the bifurcation point exists if and only if  $F > 2/3$ , which is exactly equivalent to the condition (7.23) required for linear instability of the uniform flow. A necessary condition for a limit cycle to exist is that the fixed point must be an unstable spiral, which requires that

$$1 < u_w < u_c = 1 + \frac{1}{F}. \quad (8.19)$$

Since a limit cycle will correspond to periodic roll-wave solution in physical space, the inequalities in (8.19) place a useful restriction on the range of  $u_w$ .

## 8.2. Numerical integration of the phase-plane equations

In the unstable regime, in which the Froude number  $F > 2/3$ , the phase-plane equations (8.7) and (8.8) are integrated numerically using Matlab's ode15s initial value problem solver using a prescribed value of  $u_w \in [1, u_c]$ . The integration is started from

$$(h, n) = (1.001, 0), \quad (8.20)$$

which represents a small perturbation away from the fixed point (1, 0), and the solver steps forward from  $\xi = 0$  (chosen arbitrarily). Provided a limit cycle exists, the instability causes the perturbation to grow as  $\xi$  increases until a stable roll wave is reached, as shown in figure 6(a) for the parameter values given in table 2 and a wave speed  $u_w = 1.978\,613\,807$ . Figure 6(b) shows the same solution in the phase plane, with the trajectory spiralling away from the unstable fixed point until the limit cycle is reached (the outer trajectory). When plotted in physical space the limit cycle represents a periodic roll-wave solution to the system of equations (7.1) and (7.2). It travels with speed  $u_w$ , which is always greater than the non-dimensional depth-averaged speed,  $\bar{u} = 1$ . Figure 6(c) shows three complete periods of the limit cycle in physical space. The solution computed with the new depth-averaged  $\mu(I)$ -rheology therefore looks very similar to those calculated using the inviscid theory (3.30) and (3.31), except that the discontinuous shocks are now replaced by sharply varying smooth transitions at the wavefronts.

The effect of varying  $u_w$  on the solution is shown in figure 7, where only the final limit cycle is plotted in each case. It is found that convergent solutions only exist for values of  $u_w$  close to the bifurcation point  $u_c$ , i.e. there exists a minimum wavespeed  $u_w^{min}$  for which a limit cycle exists. For each  $F$ , it is possible to iterate between the known bounds  $u_w \in [1, u_c]$  in order to find  $u_w^{min}$ . The amplitude of the roll waves increases as the wavespeed  $u_w$  is decreased away from  $u_c$  until the largest amplitude wave is reached at  $u_w = u_w^{min}$ . The overall shape of the limit cycle does not change greatly as  $u_w$  is varied.

In order to examine how the size and shape of the roll waves change with the steady-uniform Froude number, solutions are computed for various  $F$  with the wavespeed set to  $u_w = u_w^{min}$ . Recall that by (6.5), (6.6) and (7.5) the steady uniform Froude number  $F = Fr_0 = \beta h_0 / (\mathcal{L}\gamma)$ , so, at a fixed inclination, increasing  $F$  is equivalent to increasing the thickness  $h_0$  of the steady uniform flow. It is possible to plot the results in non-dimensional variables, but this can be slightly confusing, because varying  $F$ , also changes the  $h_0$  and  $\bar{u}_0$  in the non-dimensionalization (6.8). The results are therefore plotted using dimensional variables. Figure 8(a) shows the dimensional wavespeed  $u_w^{min}$ . It behaves like the bifurcation point velocity,  $u_c$ , defined in (8.18), which in dimensional variables becomes

$$u_c = \sqrt{gh_0 \cos \zeta} \left( 1 + \frac{\beta h_0}{\mathcal{L}\gamma} \right) \approx u_w^{min}, \quad (8.21)$$

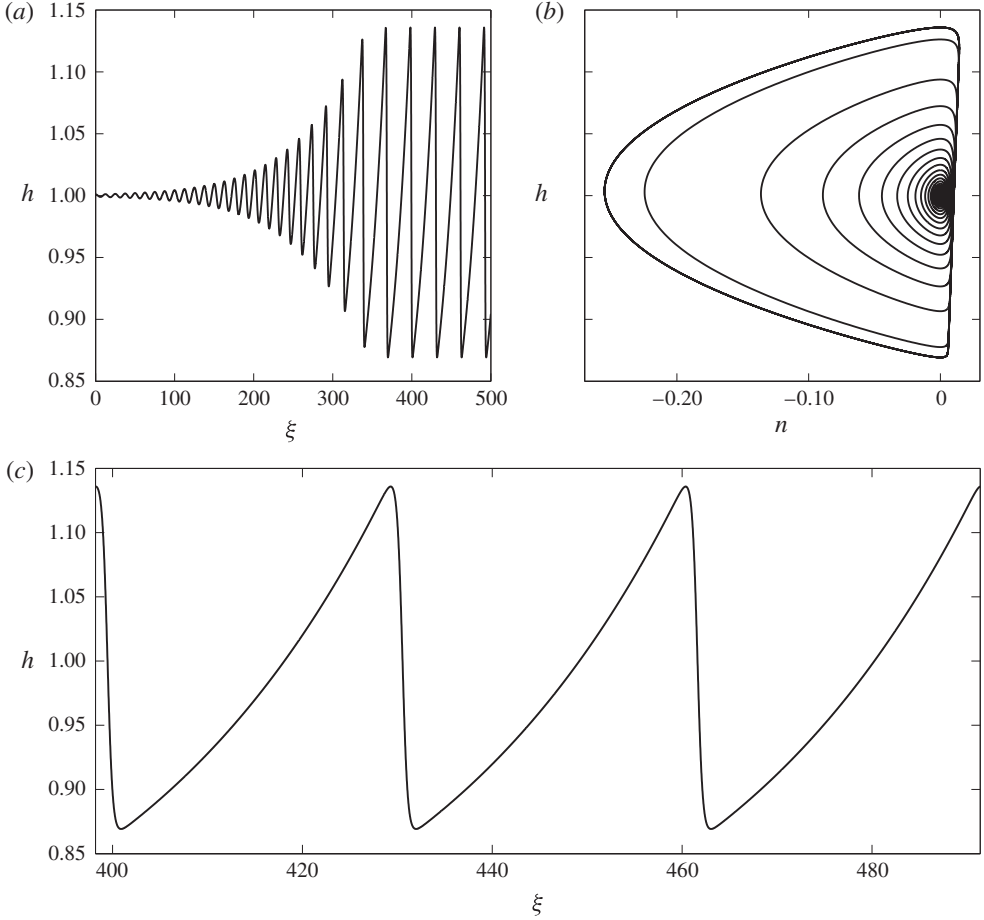


FIGURE 6. A roll-wave solution using the new depth-averaged  $\mu(I)$ -rheology for an initial condition  $(h, n) = (1.001, 0)$ , Froude number  $F = 1.02$  and wave speed  $u_w = 1.978\,613\,807$  in (a) the physical plane  $(\xi, h)$  and (b) the phase plane  $(n, h)$ . The solution in the phase plane spirals away from the fixed point and tends rapidly towards a stable limit cycle (outer trajectory). Three periods of the limit cycle are shown in (c), each one of which constitutes a single roll wave.

which has an  $h_0^{3/2}$  dependence. This suggests that for a flow that has roll waves generated at a range of  $F$ , the larger-amplitude waves will travel faster than the smaller ones, provided that they are of maximum amplitude. At any given Froude number, however, the speed of the largest amplitude wave will be slightly less than the smallest amplitude wave at the bifurcation point, as shown previously in figure 7. This difference  $\Delta u_c = u_c - u_w^{\min}$  is very small (figure 8b). Figure 8(c) shows the maximum roll-wave amplitude,  $A$ , defined here as the peak-to-trough distance, as a function of  $F$ . At the critical Froude number  $F_c = 2/3$  the amplitude is zero and  $A$  increases as  $F$  is increased. Thicker large-Froude-number flows will tend to have larger-amplitude waves, although there will also be a range of smaller-amplitude waves that are generated at the same Froude number. Figure 8(d) shows a graph of the reciprocal of the wavelength  $\Lambda$ , defined here as the peak-to-peak distance in  $\xi$ . Since  $1/\Lambda = 0$  at  $F = F_c$  the wavelength is infinite at the critical Froude number.

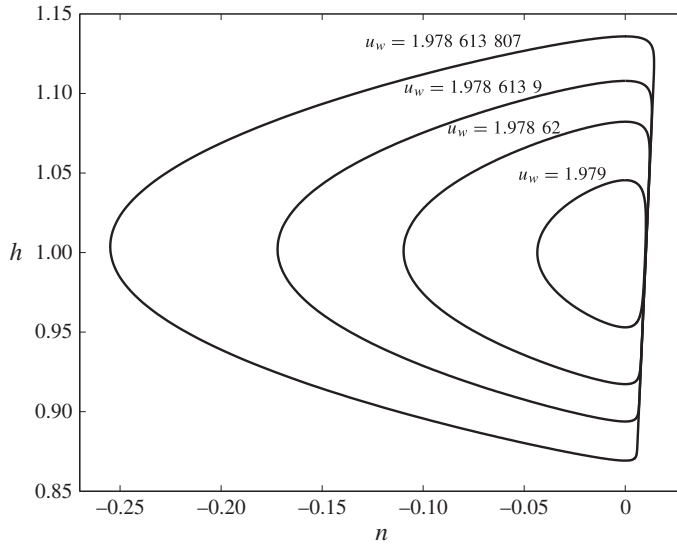


FIGURE 7. Limit cycles in the phase plane  $(n, h)$ , which correspond to roll-wave solutions using the new depth-averaged  $\mu(I)$ -rheology with parameters given in table 2. In each simulation the Froude number  $F = 1.02$  is fixed and various wave speeds  $u_w$  (labeled on the outer of the corresponding limit cycle) are prescribed.

The generation of waves with different amplitudes at each Froude number, as well as the creation of waves with differing underlying Froude numbers creates complex coarsening dynamics (see e.g. Razis *et al.* 2014) as the waves catch up with and merge with one another.

## 9. Conclusions

In this paper it is shown how the  $\mu(I)$ -rheology (Jop *et al.* 2006) can be incorporated into depth-averaged models of granular avalanches. These are extensively used for the prediction of natural hazards (e.g. Grigorian *et al.* 1967; Savage & Hutter 1989; Iverson 1997; Gray *et al.* 1999; Iverson & Denlinger 2001; Mangeney *et al.* 2007), as well as for modelling small-scale dry granular flows (e.g. Pouliquen & Forterre 2002; Gray *et al.* 2003; Johnson & Gray 2011; Cui & Gray 2013). Using the shallowness of the flow, a formal depth-integration of the mass and momentum balances yields the classical shallow-water-like avalanche equations (3.30) and (3.31). To leading order, the only effect of the rheology is to generate an effective basal friction in the source terms (3.32) that is precisely the rough bed friction law (2.8) measured by Pouliquen & Forterre (2002). The gradient of the depth-averaged in-plane deviatoric stress  $\overline{\tau_{xx}}$  does not, however, contribute to the leading-order depth-averaged momentum balance, so no viscous-like terms are generated. For most situations the classical system of avalanche equations (3.30)–(3.32) are therefore entirely appropriate.

There are some more subtle problems, such as the formation and growth of granular roll waves (Forterre & Pouliquen 2003), where a viscous-like term is required to get the correct physical behaviour. In § 4 it is shown how the  $\mu(I)$ -rheology can be approximated, using the lithostatic pressure and Bagnold velocity profiles (GDR-MiDi 2004) during the integration of the in-plane deviatoric stress,  $\tau_{xx}$ , through the avalanche thickness, to generate a viscous-like term in the depth-integrated momentum

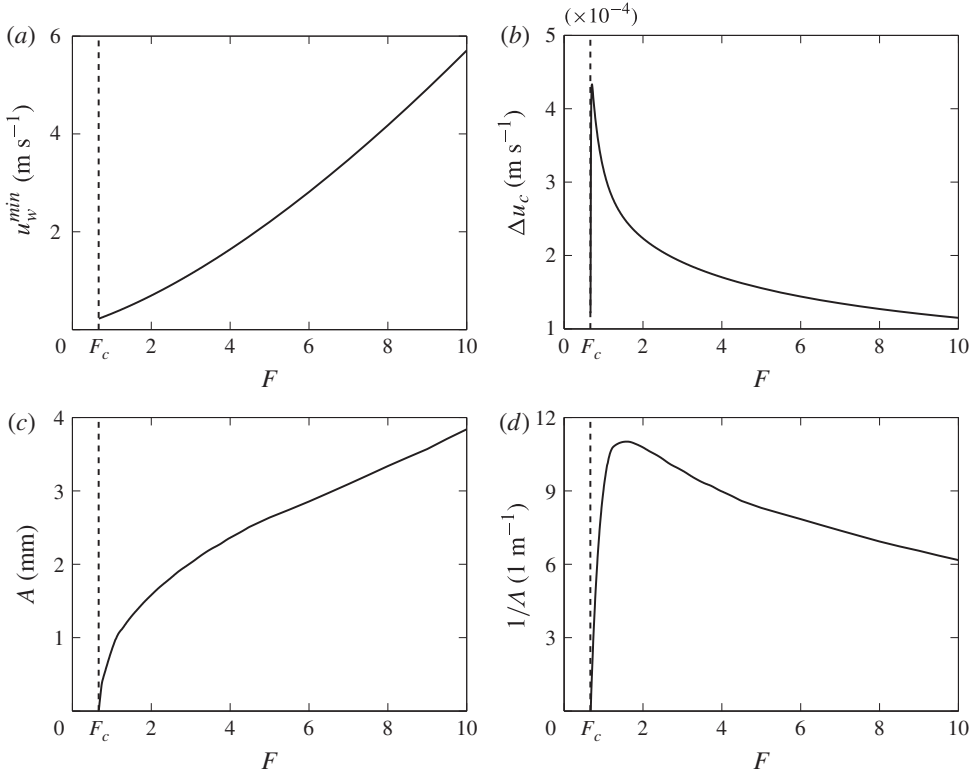


FIGURE 8. Numerical relationship (solid lines) between the Froude number  $F$  and (a) the minimum dimensional wavespeed  $u_w^{\min}$  for which there is a convergent solution (found iteratively). (b) The difference  $\Delta u_c = u_c - u_w^{\min}$  between the dimensional wavespeed at the critical point  $u_c$  given by (8.21) and the wavespeed  $u_w^{\min}$  of the largest wave for which a limit cycle exists is very small. (c,d) The corresponding dimensional amplitude  $A$  and the reciprocal wavelength  $1/\Lambda$  of the largest amplitude roll wave at a given Froude number. All results are computed for a chute inclined at an angle of  $29^\circ$ .

balance. Formally this term is  $O(\epsilon)$ , so most of the time it does not play a role and the classical equations dominate. However, the viscous term involves second-order derivatives of the depth-averaged velocity,  $\bar{u}$ , which is the highest gradient in the theory. Its inclusion in the conservation laws (4.13) and (4.14) therefore represents a singular perturbation, which plays an important role in smoothing out shocks that form with the inviscid theory, as shown for roll wavefronts in figure 6.

The new depth-averaged  $\mu(I)$ -rheology is compared with a previous depth-averaged model of Forterre (2006), which is also based on the  $\mu(I)$ -rheology. It contains a viscous-like term that involves second-order gradients of  $h\bar{u}$  and has a singularity in the viscosity as  $h \rightarrow 0$ . By considering the formation of a steadily travelling granular front on a rough inclined plane, it is shown in § 6 that Forterre's (2006) theory generates a thin precursor layer ahead of the main front. Moreover, the precise shape of the front is dependent on the depth and rate of decay of the precursor layer. Since this layer is well below the grain size of particles, this behaviour is unphysical. The new depth-averaged  $\mu(I)$ -rheology, on the other hand, does not affect the problem at all, since it is dependent on the derivative of depth-averaged velocity

$\bar{u}$ , which is zero. The inviscid solution, with a clearly defined frontal shape and a completely grain-free region ahead of the front, is therefore reproduced exactly.

A linear stability analysis using the new depth-averaged  $\mu(I)$ -rheology predicts that steady-uniform flows become unstable above a critical Froude number  $F_c = 2/3$ . The spatial growth rate and phase velocity are in very good agreement with the experimental results of Forterre & Pouliquen (2003), without the use of any fitting parameters. In particular, the new model predicts a cutoff frequency,  $\omega_c$ , that is in excellent agreement with experimental results over a wide range of slope inclination angles,  $\zeta$ , and Froude numbers,  $F$ , as shown in figure 5. The agreement is at least as good as the instability results of the full  $\mu(I)$ -rheology in two dimensions (Forterre 2006). It is certainly an improvement on the inviscid model, which does not predict cutoff at all, as well as the depth-averaged model of Forterre (2006), which required an additional arbitrary fitting parameter. The near independence of the cutoff frequency,  $\omega_c$ , on the slope inclination angle is a direct consequence of the dependence of the coefficient,  $\nu$  (defined in (4.16)), on the slope inclination angle,  $\zeta$ . The stability results therefore provide strong evidence that the increase in  $\nu$  as the inclination angle,  $\zeta$ , decreases, is an important physical effect that may play a significant role in flow arrest processes. Indeed as  $\zeta$  tends to the minimum angle,  $\zeta_1$ , for steady-uniform flow the effective viscosity  $\nu h^{3/2}/2$  tends to infinity. Conversely as  $\zeta$  tends to the maximum angle for steady-uniform flow,  $\zeta_2$  the effective viscosity tends to zero. Outside this range, the viscosity is negative, which will lead to ill-posedness. Bizarrely this is also consistent with the full  $\mu(I)$ -rheology, which is ill-posed for very high and very low values of the inertial number (Barker *et al.* 2014). A simple regularization of the depth-averaged  $\mu(I)$ -rheology can be achieved by setting a maximum and minimum threshold for the coefficient,  $\nu$ , which is positive for all inclination angles, as shown in figure 2. This regularization has not, however, been used in this paper, because the comparisons with experimental data are all done in the well-posed region of parameter space.

## Acknowledgements

This research was supported by NERC grants NE/E003206/1 and NE/K003011/1 as well as EPSRC grants EP/I019189/1 and EP/K00428X/1. N. Gray acknowledges support from the program on ‘Fluid-Mediated Particle Transport in Geophysical Flows’ at the Kavli Institute for Theoretical Physics, S. Barbara, USA, and A. Edwards acknowledges support from NERC Doctoral Training Grant NE/G523747/1. The authors would like to thank D. Schaeffer and P. Kokelaar for many enlightening discussions.

## REFERENCES

- ABRAMOWITZ, M. & STEGUN, I. 1970 *Handbook of Mathematical Functions*, 9th edn. p. 3.3.7. Dover.
- ANCEY, C., COUSSOT, P. & EVESQUE, P. 1999 A theoretical framework for granular suspensions in a steady simple shear flow. *J. Rheol.* **43** (6), 1673–1699.
- BARBOLINI, M., DOMAAS, U., FAUG, T., GAUER, P., HÁKONARDÓTTIR, K. M., HARBITZ, C. B., ISSLER, D., JÓHANNESSEN, T., LIED, K., NAAIM, M., NAAIM-BOUVET, F. & RAMMER, L. 2009 EUR 23339 – the design of avalanche protection dams – recent practical and theoretical developments. European Commission.
- BARKER, T., SCHAEFFER, D. G., BOHÓRQUEZ, P. & GRAY, J. M. N. T. 2014 Well-posed and ill-posed behaviour of the  $\mu(I)$ -rheology for granular flow. *J. Fluid Mech.* (submitted).



- BOUCHUT, F. & WESTDICKENBERG, M. 2004 Gravity driven shallow water models for arbitrary topography. *Commun. Math. Sci.* **2**, 359–389.
- CHRISTEN, M., KOWALSKI, J. & BARTELT, P. 2010 Ramms: numerical simulation of dense snow avalanches in three-dimensional terrain. *Cold Reg. Sci. Technol.* **63**, 1–14.
- CUI, X. & GRAY, J. M. N. T. 2013 Gravity-driven granular free-surface flow around a circular cylinder. *J. Fluid Mech.* **720**, 314–337.
- CUI, X., GRAY, J. M. N. T. & JÓHANNESSON, T. 2007 Deflecting dams and the formation of oblique shocks in snow avalanches at Flateyri, Iceland. *J. Geophys. Res.* **112**, F04012.
- DENLINGER, R. P. & IVERSON, R. M. 2001 Flow of variably fluidized granular masses across three-dimensional terrain: 2. Numerical predictions and experimental tests. *J. Geophys. Res.* **106** (B1), 553–566.
- DOYLE, E. E., HOGG, A. J. & MADER, H. 2011 A two-layer approach to modelling the transformation of dilute pyroclastic currents into dense pyroclastic flows. *Proc. R. Soc. A* **467** (2129), 1348–1371.
- FISCHER, J. T., KOWALSKI, J. & PUDASAINI, S. 2012 Topographic curvature effects in applied avalanche modeling. *Cold Reg. Sci. Technol.* **74–75**, 21–30.
- FORTERRE, Y. 2006 Kapiza waves as a test for three-dimensional granular flow rheology. *J. Fluid Mech.* **563**, 123–132.
- FORTERRE, Y. & POULIQUEN, O. 2003 Long-surface-wave instability dense granular flows. *J. Fluid Mech.* **486**, 21–50.
- GDR-MiDi, 2004 On dense granular flows. *Eur. Phys. J. E* **14**, 341–365.
- GOLDHIRSCH, I. 2003 Rapid granular flows. *Annu. Rev. Fluid Mech.* **35** (1), 267–293.
- GRAY, J. M. N. T. & ANCEY, C. 2009 Segregation, recirculation and deposition of coarse particles near two-dimensional avalanche fronts. *J. Fluid Mech.* **629**, 387–423.
- GRAY, J. M. N. T. & CUI, X. 2007 Weak, strong and detached oblique shocks in gravity driven granular free-surface flows. *J. Fluid Mech.* **579**, 113–136.
- GRAY, J. M. N. T. & KOKELAAR, B. P. 2010a Large particle segregation, transport and accumulation in granular free-surface flows. *J. Fluid Mech.* **652**, 105–137.
- GRAY, J. M. N. T. & KOKELAAR, B. P. 2010b Large particle segregation, transport and accumulation in granular free-surface flows—erratum. *J. Fluid Mech.* **657**, 539.
- GRAY, J. M. N. T., TAI, Y. C. & NOELLE, S. 2003 Shock waves, dead-zones and particle-free regions in rapid granular free-surface flows. *J. Fluid Mech.* **491**, 161–181.
- GRAY, J. M. N. T., WIELAND, M. & HUTTER, K. 1999 Free surface flow of cohesionless granular avalanches over complex basal topography. *Proc. R. Soc. A* **455**, 1841–1874.
- GREVE, R. & HUTTER, K. 1993 Motion of a granular avalanche in a convex and concave curved chute: experiments and theoretical predictions. *Phil. Trans. R. Soc. Lond. A* **342**, 573–600.
- GRIGORIAN, S. S., EGLIT, M. E. & IAKIMOV, I. L. 1967 New state and solution of the problem of the motion of snow avalanche. *Snow, Avalanches & Glaciers. Tr. Vysokogornogo Geofizich Inst.* **12**, 104–113.
- HÁKONARDÓTTIR, K. M. & HOGG, A. J. 2005 Oblique shocks in rapid granular flows. *Phys. Fluids* **17**, 0077101.
- IVERSON, R. M. 1997 The physics of debris-flows. *Rev. Geophys.* **35**, 245–296.
- IVERSON, R. M. & DENLINGER, R. P. 2001 Flow of variably fluidized granular masses across three-dimensional terrain 1. Coulomb mixture theory. *J. Geophys. Res.* **106** (B1), 553–566.
- JENKINS, J. T. & SAVAGE, S. B. 1983 A theory for the rapid flow of identical, smooth, nearly elastic, spherical-particles. *J. Fluid Mech.* **130**, 187–202.
- JOHNSON, C. G. & GRAY, J. M. N. T. 2011 Granular jets and hydraulic jumps on an inclined plane. *J. Fluid Mech.* **675**, 87–116.
- JOP, P., FORTERRE, Y. & POULIQUEN, O. 2005 Crucial role of sidewalls in granular surface flows: consequences for the rheology. *J. Fluid Mech.* **541**, 167–192.
- JOP, P., FORTERRE, Y. & POULIQUEN, O. 2006 A constitutive relation for dense granular flows. *Nature* **44**, 727–730.
- JORDAN, D. W. & SMITH, P. 1987 *Nonlinear Ordinary Differential Equations*. Oxford University Press.

- KUO, C., TAI, Y. C., BOUCHUT, F., MANGENEY, A., PELANTI, M., CHEN, R. & CHANG, K. 2009 Simulation of Tsaoiling landslide, Taiwan, based on Saint Venant equations over general topography. *Engng Geol.* **104** (3–4), 181–189.
- LAGRÉE, P.-Y., STARON, L. & POPINET, S. 2011 The granular column collapse as a continuum: validity of a two-dimensional Navier–Stokes model with a  $\mu(I)$ -rheology. *J. Fluid Mech.* **686**, 378–408.
- LUCA, I., HUTTER, K., TAI, Y. C. & KUO, C. Y. 2009 A hierarchy of avalanche models on arbitrary topography. *Acta Mechanica* **205**, 121–149.
- MAJMUDAR, T. S. & BEHRINGER, R. P. 2005 Contact force measurements and stress-induced anisotropy in granular materials. *Nature* **435**, 1079–1082.
- MANGENEY, A., BOUCHUT, F., THOMAS, N., VILOTTE, J. P. & BRISTEAU, M. O. 2007 Numerical modeling of self-channeling granular flows and of their levee-channel deposits. *J. Geophys. Res.* **112**, F02017.
- MANGENEY, A., ROCHE, O., HUNGR, O., MANGOLD, N., FACCANONI, G. & LUCAS, A. 2010 Erosion and mobility in granular collapse over sloping beds. *J. Geophys. Res.* **115**, F03040.
- MANGENEY-CASTELNAU, A., VILOTTE, J. P., BRISTEAU, M. O., PERTHAME, B., BOUCHUT, F., SIMEONI, C. & YERNENI, S. 2003 Numerical modeling of avalanches based on Saint-Venant equations using a kinetic scheme. *J. Geophys. Res.* **108**, 2527–2544.
- NEEDHAM, D. J. & MERKIN, J. H. 1984 On roll waves down an open inclined channel. *Proc. R. Soc.* **394**, 259–278.
- PITMAN, E. B., NICHITA, C. C., PATRA, A., BAUER, A., SHERIDAN, M. & BURSIK, M. 2003 Computing granular avalanches and landslides. *Phys. Fluids* **15** (12), 3638–3646.
- POULIQUEN, O. 1999a Scaling laws in granular flows down rough inclined planes. *Phys. Fluids* **11** (3), 542–548.
- POULIQUEN, O. 1999b On the shape of granular fronts down rough inclined planes. *Phys. Fluids* **11** (7), 1956–1958.
- POULIQUEN, O., DELOUR, J. & SAVAGE, S. B. 1997 Fingering in granular flows. *Nature* **386**, 816–817.
- POULIQUEN, O. & FORTERRE, Y. 2002 Friction law for dense granular flows: application to the motion of a mass down a rough inclined plane. *J. Fluid Mech.* **453**, 133–151.
- POULIQUEN, O. & VALLANCE, J. W. 1999 Segregation induced instabilities of granular fronts. *Chaos* **9** (3), 621–630.
- PUDASAINI, S. P. & HUTTER, K. 2003 Rapid shear flows of dry granular masses down curved and twisted channels. *J. Fluid Mech.* **495**, 193–208.
- RAZIS, D., EDWARDS, A. N., GRAY, J. M. N. T. & VAN DER WEELE, K. 2014 Arrested coarsening of granular roll waves. *Phys. Fluids* (submitted).
- SAMPL, P. & ZWINGER, T. 2004 Avalanche simulation with SAMOS. *Ann. Glaciol.* **38** (1), 393–398.
- SAVAGE, S. B. 1984 The mechanics of rapid granular flows. *Adv. Appl. Mech.* **24**, 289–366.
- SAVAGE, S. B. & HUTTER, K. 1989 The motion of a finite mass of granular material down a rough incline. *J. Fluid Mech.* **199**, 177–215.
- SAVAGE, S. B. & HUTTER, K. 1991 The dynamics of avalanches of granular materials from initiation to run-out. I. Analysis. *Acta Mechanica* **86**, 201–223.
- SOVILLA, B., SCHAEER, M., KERN, M. & BARTELT, P. 2008 Impact pressures and flow regimes in dense snow avalanches observed at the Vallée de la Sionne test site. *J. Geophys. Res.* **113**, F01010.
- STARON, L., LAGRÉE, P.-Y. & POPINET, S. 2012 The granular silo as a continuum plastic flow: the hour-glass vs the clepsydra. *Phys. Fluids* **24**, 103301.
- STROGATZ, S. H. 1994 *Nonlinear Dynamics and Chaos*. Westview Press.
- TAI, Y. C., NOELLE, S., GRAY, J. M. N. T. & HUTTER, K. 2002 Shock-capturing and front-tracking methods for granular avalanches. *J. Comput. Phys.* **175**, 269–301.
- VREMAN, A. W., AL-TARAZI, M., KUIPERS, J. A. M., SINT, M. V. & BOKHOVE, O. 2007 Supercritical shallow granular flow through a contraction: experiment, theory and simulation. *J. Fluid Mech.* **578**, 233–269.

- WIELAND, M., GRAY, J. M. N. T. & HUTTER, K. 1999 Channelised free surface flow of cohesionless granular avalanches in a chute with shallow lateral curvature. *J. Fluid Mech.* **392**, 73–100.
- WOODHOUSE, M. J., THORNTON, A. R., JOHNSON, C. G., KOKELAAR, B. P. & GRAY, J. M. N. T. 2012 Segregation-induced fingering instabilities in granular free-surface flows. *J. Fluid Mech.* **709**, 543–580.
- WU, W., BAUER, E. & KOLYMBAS, D. 1996 Hypoplastic constitutive model with critical state for granular materials. *Mech. Mater.* **23** (1), 45–69.